


Review

# Review of Turbine Parameterization Models for Large-Eddy Simulation of Wind Turbine Wakes

Zhaobin Li <sup>1,2</sup>, Xiaohao Liu <sup>1,2,\*</sup> and Xiaolei Yang <sup>1,2,\*</sup> 

<sup>1</sup> The State Key Laboratory of Nonlinear Mechanics, Institute of Mechanics, Chinese Academy of Sciences, Beijing 100190, China

<sup>2</sup> School of Engineering Sciences, University of Chinese Academy of Sciences, Beijing 100049, China

\* Correspondence: xyang@imech.ac.cn

**Abstract:** Wind turbine parameterization models, which are often employed to avoid the computational cost of resolving the blade aerodynamics, are critical for the capability of large-eddy simulation in predicting wind turbine wakes. In this paper, we review the existing wind turbine parameterization models, i.e., the actuator disk model, the actuator line model, and the actuator surface model, by presenting the fundamental concepts, some advanced issues (i.e., the force distribution approaches, the method for velocity sampling, and the tip loss correction), and their applications to utility-scale wind farms. Emphasis is placed on the predictive capability of different parameterizations for different wake characteristics, such as the blade load, the tip vortices and hub vortex in the near wake, and the meandering of the far wake. The literature demonstrated the importance of taking into account the effects of nacelle and tower in wind turbine wake predictions. The predictive capability of the actuator disk model with different model complexities, which is preferred in wind farm simulations, is systematically reviewed for different inflows and different wind turbine designs. Applications to wind farms show good agreements between simulation results and measurements.

**Keywords:** wind turbine wake; large-eddy simulation; turbine parameterization; actuator disk; actuator line; actuator surface



**Citation:** Li, Z.; Liu, X.; Yang, X.

Review of Turbine Parameterization Models for Large-Eddy Simulation of Wind Turbine Wakes. *Energies* **2022**, *15*, 6533. <https://doi.org/10.3390/en15186533>

Academic Editor: Davide Astolfi

Received: 17 August 2022

Accepted: 5 September 2022

Published: 7 September 2022

**Publisher's Note:** MDPI stays neutral with regard to jurisdictional claims in published maps and institutional affiliations.



**Copyright:** © 2022 by the authors. Licensee MDPI, Basel, Switzerland. This article is an open access article distributed under the terms and conditions of the Creative Commons Attribution (CC BY) license (<https://creativecommons.org/licenses/by/4.0/>).

## 1. Introduction

While wind turbines extract the kinetic energy from wind, they leave behind a wake featured by low wind speed and high turbulence intensity, which can reduce the power and increase the fatigue loads of their downwind neighbors [1,2]. Understanding the wake evolution is thus crucial for the design, operation, and optimization of the wind farm as a whole. Computational fluid dynamics (CFD) provides an efficient approach for studying wake dynamics under controlled conditions. However, using blade-resolved approaches for simulating wind turbine wakes is still challenging. On one hand, these simulations are prohibitively expensive if not impossible, because of the wide range of length scales involved in the fluid dynamics, ranging from several centimeters for the boundary layer thickness of the blade to several kilometers for the wake length of a wind farm. This computational challenge is even more severe if the deformation of the modern slender wind turbine blade has to be considered in blade-resolved fluid-structure interaction simulations. On the other hand, blade-resolved simulations require precise blade geometry detail, which is often proprietary (not available to the public), introducing uncertainties in blade-resolved simulations as the employed blade geometry cannot be exactly the same as the real one. To this regard, parameterization models of wind turbines, which represent the blade aerodynamics via distributed forces based on minimal blade information, offer an efficient and practical approach for wind turbine wake simulations [3,4].

Three types of turbine parameterization models are commonly employed by the community, i.e., the actuator disk (AD) model, the actuator line (AL) model, and the actuator surface (AS) model. As shown in Figure 1, these models exert actuator forces

on the surrounding flow to mimic the effect of a wind turbine. Each model differs from other ones by the way how the forces are computed and applied to the fluid, thus offering a unique efficiency and predictive capability. Actuator wind turbine models are frequently employed, implemented either with Reynolds-Averaged Navier–Stokes (RANS) methods or large-eddy simulation (LES) methods [5–7]. A literature survey shows that the community has converged on a consensus that LES is most appropriate for predicting the unsteadiness and turbulence structures in wind turbine wakes. In LES of wind turbine wakes, different variants of turbine parameterization models have been developed [8–10]. In this paper, we attempt to provide a general guideline for selecting and setting up these parameterization models, taking into account the levels of sophistication of the models, their efficiency, and their predictive capabilities for different quantities of interest.

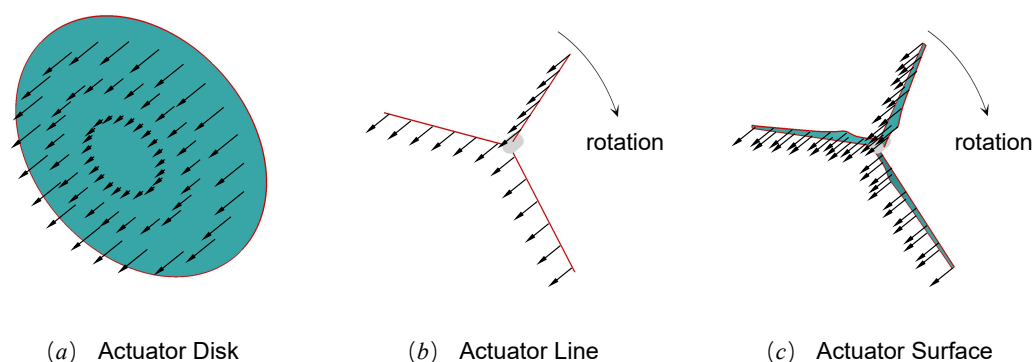


**Figure 1.** Wind turbine rotor parameterization models for wake simulations with computational fluid dynamics approaches. (a) AD model: the rotor is simplified as a thin round disk of the same size as the rotor-swept area; (b) AL model: the blades are simplified as lines; (c) AS model: the blades are simplified with zero thickness surfaces defined by the blade’s chord and twist angle.

Specifically, one objective of this work is to provide a guideline for choosing these models according to their predictive capability and computational cost, through a comprehensive survey of literature on the validation works and typical applications. The second objective is to outline the fine-tuning issues to show how the model parameters influence the prediction accuracy. These fine-tuning techniques include the tip-loss correction, the body force distribution, and the reference velocity sampling.

The paper is structured into six sections. After this short introduction, Section 2 recalls the fundamentals of the wind turbine parameterization models. Section 3 discusses the advanced numerical issues mentioned above. The predictive capability of these models is compared in Section 4 by a survey of literature on model validation and model-to-model comparison. Section 5 provides the typical applications of these models before the last section for a summary of this review.

## 2. Fundamentals of Turbine Parameterization Models

### 2.1. Governing Equations of the Flow Field

The most common choice for describing the flow around wind turbines are the filtered Navier–Stokes equations for incompressible flow,

$$\frac{\partial \tilde{u}_i}{\partial x_i} = 0, \quad (1)$$

$$\frac{\partial \tilde{u}_i}{\partial t} + \tilde{u}_j \frac{\partial \tilde{u}_i}{\partial x_j} = -\frac{1}{\rho} \frac{\partial \tilde{p}}{\partial x_i} + \nu \frac{\partial^2 \tilde{u}_i}{\partial x_j \partial x_j} - \frac{\partial \tau_{ij}}{\partial x_j} + f_i^e, \quad (2)$$

where  $i, j = 1, 2, 3$  are the directional indices,  $u_i$  are the velocity components,  $p$  is the pressure,  $\nu$  is the kinematic viscosity,  $\tilde{\cdot}$  is the spatial filtering operator.  $\tau_{ij}$  is the residual-stress tensor resulting from the filtering process, which is defined as follows,

$$\tau_{ij} = \widetilde{u_i u_j} - \tilde{u}_i \tilde{u}_j, \quad (3)$$

and modeled using the subgrid-scale closure models, e.g., the dynamic Smagorinsky model [11]. In Equation (2),  $f_i^e$  represents the distributed body force due to the wind turbine parameterization models.

## 2.2. Actuator Disk Model

As illustrated by Figure 1a, the AD model represents the wind turbine rotor with a round thin stationary disk the same as the rotor-swept area. The action of the rotor on the flow is represented with an equivalent thrust  $T$ . The actuator disk concept has a long history dating back to Froude [12] and lays the foundation for several important theories of rotor dynamics, e.g., the one-dimensional momentum theory and the Betz limit [13,14], long before being employed in LES.

According to the one-dimensional momentum theory, the thrust coefficient  $C_T$  and the power coefficient  $C_P$  are related to the axial induction factor  $a$  as follows:

$$C_T \equiv \frac{T}{1/2\rho U_\infty^2 A} = 4a(1-a), \quad (4)$$

and

$$C_P \equiv \frac{P}{1/2\rho U_\infty^3 A} = 4a(1-a)^2, \quad (5)$$

where  $T$  and  $P$  are the thrust and the power, respectively.  $\rho$  is the air density,  $U_\infty$  is the freestream velocity,  $A = \pi R^2$  is the rotor-swept area and  $R$  is the rotor radius.

For turbine array simulations, in which the incoming wind speed is not well defined, the following relation can be employed,

$$U_\infty = \frac{U_d}{1-a}, \quad (6)$$

where  $U_d$  is the velocity on the disk. However, it is noticed that the above relations cannot be applied to heavily loaded rotors ( $C_T > 1$ ,  $a > 1/2$ ) or for unsteady wake states [15–17], for which one can apply certain corrections with the help from blade-resolved simulations, measurements, and theoretical analysis.

In the early days, the focal point of the AD model was on the power and near wake prediction. For example, the unsteady AD model of Sørensen et al. [18] was designed to solve the transient power due to blade pitching operation [19] and the turbulent wake state of a heavily loaded rotor [20]. Later, the far wake evolution also received attention using RANS method [21]. In LES, the AD model employed by Jimenez et al. [22] for predicting the wake of a wind turbine immersed in an atmospheric turbulent boundary layer, which has become a popular tool in the wind energy science community to reveal the complex wake dynamics. Two types of AD model are frequently employed, i.e., the one with a uniform thrust distribution and the other one non-uniform loaded.

### 2.2.1. Actuator Disk Model with Uniform Thrust

The AD model with evenly distributed thrust over the disk is the simplest but also the most widely employed wind turbine parameterization model. This model ignores the radial variation of the thrust along the blade and also the tangential forces, acting as a permeable drag disk.

The thrust  $T$  is computed using the thrust coefficient  $C_T$  as follows,

$$T = \frac{1}{2} \rho C_T U_\infty^2 A, \quad (7)$$

where  $C_T$  is the input parameter defining the rotor's operational status.

Equation (7) can be employed directly for a stand-alone wind turbine, where the inflow velocity  $U_\infty$  is well defined [22]. For a wind turbine positioned in the wake of its upwind neighbors, the incoming wind speed  $U_\infty$  is not well defined [23–25]. In these cases, the thrust can be computed as follows,

$$T = \frac{1}{2} \rho C'_T U_d^2 A, \quad (8)$$

which is derived using Equation (6). In the above equation, the velocity  $U_d$  on the disk is well defined and can be obtained easily. The modified thrust coefficient  $C'_T$  is defined as follows,

$$C'_T = \frac{C_T}{(1-a)^2}, \quad (9)$$

which enables its applications in turbine array simulations. Note that Equations (7) and (8) are equivalent only if the one-dimensional momentum theory is valid so that it is only applicable for  $C_T < 1$  (which is often the case for wind turbine rotor).

### 2.2.2. Actuator Disk Model with Non-Uniform Thrust and Tangential Force

More sophisticated AD models take the radial variations of the thrust and the tangential force into account. When the blade information is known, the force can be computed based on the blade element momentum (BEM) theory [26], as in the model developed by Wu and Porté-Agel [27].

For cases without the blade information, Sørensen et al. [28] proposed analytical formulae to estimate the axial and the tangential forces, based on simple input parameters such as the rotor radius, tip speed ratio, and thrust coefficient with the assumption that the circulation  $\Gamma_0$  is constant along the blade. In their formulation, the dimensionless axial and tangential forces are computed as follows:

$$\frac{f_a}{\rho U_\infty^2} = q_0 \frac{gF}{r^+} \left( \lambda r^+ + \frac{1}{2} q_0 \frac{gF}{r^+} \right), \quad (10)$$

$$\frac{f_t}{\rho U_\infty^2} = \frac{U_D}{U_\infty} q_0 \frac{gF}{r^+}, \quad (11)$$

where  $U_\infty$  is the incoming velocity,  $r^+ = r/R$  is the dimensionless radius,  $q_0 = \frac{\Gamma_0}{4\pi R U_\infty}$  is the dimensionless circulation, and  $\lambda = \Omega R / U_\infty$  is the tip speed ratio.  $F = F(r^+)$  is the tip correction function, and  $g = g(r^+)$  is the root correction function. The reader is referred to ref. [28] for a complete description of these functions.

Either using the blade information or the analytical formulae, the incoming reference velocity  $U_\infty$  is required. For a stand-alone wind turbine,  $U_\infty$  is simply defined as the freestream velocity. For a turbine in an array,  $U_\infty$  can be computed as follows:

$$U_\infty = \frac{2U_D}{1 + \sqrt{1 - C_T}}. \quad (12)$$

It is noticed that the above relation is the same with Equation (6) when  $C_T = 4a(1-a)$ . The forces employed in the AD model can be given by more advanced models as well, especially when one wants to investigate the predictive capability of the AD model [29,30].

### 2.3. Actuator Line Model

The AL model represents the blade of the rotor using a rotating line with distributed forces as shown in Figure 1b. This method was proposed by Sørensen and Shen [8] to

predict the load, the power, and the near wake of a rotor. The advantage of the AL model is that the discrete tip vortices in the near wake can be captured, in contrast to the AD model where the rotor is assumed to have an infinite number of blades. The following subsections detail the fundamental concept of the AL model.

### 2.3.1. Basic Formulation

The AL model employs the blade element method [31] to compute the forces on the blade. The method divides a blade into a number of elements in the spanwise direction and the aerodynamic force is computed element by element with the two-dimensional airfoil dataset.

Figure 2 shows an illustration of the blade element concept. The  $x$  and  $\theta$  represent the axial and the blade rotational directions, respectively.  $\mathbf{U}_{\text{rel}}$  is the incoming velocity relative to the moving blade element, which can be decomposed into an axial component  $U_D(r)$  and a tangential component  $W_D(r) + \Omega r$ , with  $\Omega$  the rotor rotating velocity.

$$\mathbf{U}_{\text{rel}}(r) = U_D(r)\mathbf{e}_x - (\Omega r + W_D(r))\mathbf{e}_\theta, \quad (13)$$

where  $\mathbf{e}_x$  and  $\mathbf{e}_\theta$  denote the unit vectors in the axial and tangential directions, respectively.

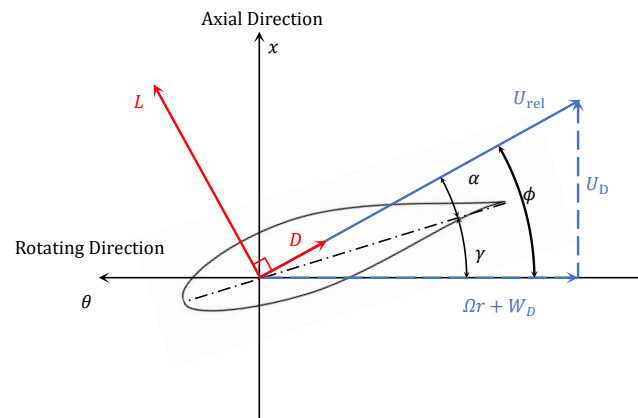


**Figure 2.** A two-dimensional cross-section of a blade for computing the lift and drag forces in the actuator line model.

The angle of attack  $\alpha$  is defined as

$$\alpha = \phi - \gamma. \quad (14)$$

where  $\gamma$  is the local pitch of the airfoil (due to the blade twist and the control), i.e., the angle between the plane of rotation and the chord (dashed-point line in Figure 2) and  $\phi$  is the angle between  $\mathbf{U}_{\text{rel}}$  and the plane of rotation.

The lift ( $L$ ) and the drag ( $D$ ) per unit span of the two-dimensional blade section are computed with

$$L = \frac{1}{2} \rho c C_L(\alpha) \mathbf{U}_{\text{rel}}^2, \quad (15)$$

and

$$D = \frac{1}{2} \rho c C_D(\alpha) \mathbf{U}_{\text{rel}}^2, \quad (16)$$

where  $c$  denotes the airfoil chord length.  $C_L(\alpha)$  and  $C_D(\alpha)$  are the lift and drag coefficients, which can be obtained from wind tunnel experiments or numerical simulations. It is noticed that  $C_L$  and  $C_D$  are also functions of the Reynolds number, which are not discussed in this paper. The thrust and tangential forces on each blade element are then computed as follows,

$$dT = (L \cos \phi + D \sin \phi) dr, \quad (17)$$

$$dF_t = (L \sin \phi - D \cos \phi) dr, \quad (18)$$

with  $dr$  the length of the blade element.

### 2.3.2. Corrections for Three-Dimensional Aerodynamic Effects

In the basic AL model (as well as other methods based on the blade element method), there is a strong simplification that the three-dimensional effects on the lift and drag coefficients are not accounted for. These three-dimensional aerodynamic effects are related to both rotor rotation and blade geometry. For example, the rotation was found to augment the lift in wind tunnel measurement [32], while the blade taper near the tip leads to a decreased aerodynamic force near the blade extremity [33]. The following content describes the correction for the stall delay of rotating blades. The tip-loss correction, on which there are some controversial debates, is discussed in detail in Section 3.3.

The three-dimensional (3D) stall delay corrections were proposed by several authors in the literature, e.g., Du and Selig [34] and Chaviaropoulos and Hansen [35]. For the sake of brevity, the 3D stall correction formulated by Du and Selig [34] is provided in the following as an example,

$$C_{L,3D} = C_{L,2D} + f_L(C_{L,p} - C_{L,2D}), \quad (19)$$

and

$$C_{D,3D} = C_{D,2D} - f_D(C_{D,2D} - C_{D,0}), \quad (20)$$

where  $C_{L,3D}$  and  $C_{D,3D}$  are the corrected coefficients of the lift and the drag, respectively,  $C_{L,p} = 2\pi(\alpha - \alpha_0)$  is the linear potential solution of the lift coefficient of the two-dimensional blade section, and  $C_{D,0}$  is the drag coefficient at zero angle of attack. The  $f_L$  and  $f_D$  are coefficients obtained by fitting the experimental data, which are expressed as follows

$$f_L = \frac{1}{2\pi} \left( \frac{1.6(c/r) a - (c/r) \frac{d}{\Lambda} \frac{R}{r}}{0.1267 b + (c/r) \frac{d}{\Lambda} \frac{R}{r}} - 1 \right), \quad (21)$$

and

$$f_D = \frac{1}{2\pi} \left( \frac{1.6(c/r) a - (c/r) \frac{d}{2\Lambda} \frac{R}{r}}{0.1267 b + (c/r) \frac{d}{2\Lambda} \frac{R}{r}} - 1 \right), \quad (22)$$

respectively.  $\Lambda = \Omega R / \sqrt{\Omega^2 R^2 + U_\infty^2}$  is the modified tip speed ratio. The default values of  $a$ ,  $b$ , and  $d$  are equal to unity.

### 2.4. Actuator Surface Model

The AS model employs a rotating two-dimensional load-carrying surface to represent the rotor blade as shown in Figure 1c. Several different implementations of the AS model were found in the literature, including Dobrev et al. [36], Shen et al. [9], Sibuet Watters et al. [37], Yang and Sotiropoulos [10]. In these AS methods, the surface geometry explicitly expressed the chord and local twist angle, only neglecting the blade thickness. The advantage of the AS model is that it allows a more realistic representation of the blade geometry and the load distribution in the chordwise direction, in contrast to the AL model. Specifically, the force in the AS model can be computed in the same way as the AL method, but its chordwise distribution is required in extra, as follows,

$$f_{AS}(r, \xi) = f_{AL}(r)F(\xi) \quad (23)$$

where  $f_{AS}(r, \xi)$  is the distributed force on the actuator surface,  $r$  is the radial location, and  $\xi$  denotes the distance to the leading edge in the chordwise direction,  $f_{AL}(r)$  is the integrated load of the airfoil section, and  $F(\xi)$  is the chordwise distribution. A number of distribution functions have been proposed to spread the blade load in the chordwise direction (see Figure 3), including the piece-wise linear distribution of Dobrev et al. [36] and

Kim et al. [38], the data-fitted distribution Shen et al. [9,39], and the constant distribution of Yang and Sotiropoulos [10]. Apparently, the piece-wise linear and the constant distributions are simple and convenient to implement. The data-fitted distribution, on the other hand, needs to fit a number of empirical parameters based on two-dimensional airfoil simulations. Refs. [9,36] compared the flow field around an airfoil predicted by the AS model with that from the geometry-resolved simulation, obtaining a fairly good agreement.

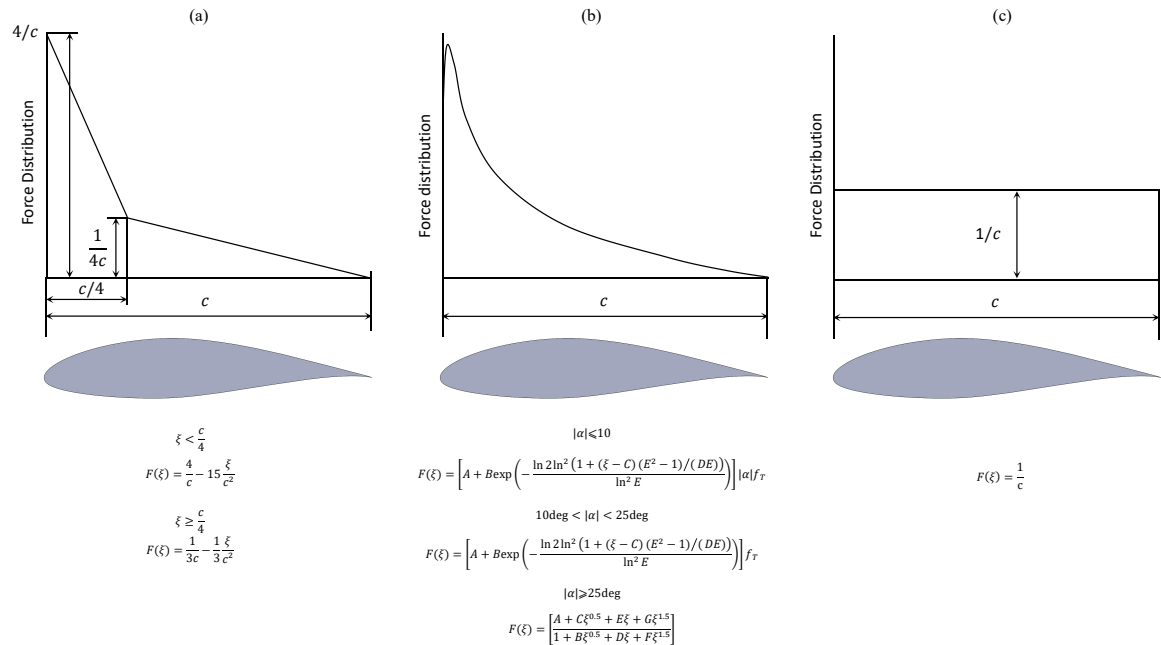


**Figure 3.** Examples of chordwise distribution of the blade load in the AS model for (a) piece-wise linear distribution [36], (b) data-fitted distribution [9], and (c) constant distribution [10].

From the wake simulation point of view, the AS model ameliorates the accuracy of the near wake, resulting in a more precise initial condition for the downstream wake evolution. For this reason, the choice of force distribution depends on how precise the flow dynamics need to be resolved. When the focus is the flow around the airfoil or the very near wake of a wind turbine (at a downstream distance of several blade chord lengths), the force distributions that function closest to the real one are preferred, incorporating an adequately refined grid around the blades. However, fine grid resolution may become infeasible for wind-farm-scale simulations, so simple force distributions are sufficient for these cases when the wake dynamics are of interest. In the literature [10,40], it was shown that the AS model with a constant force distribution is able to predict the near wake characteristics and meandering of the far wake accurately, and the proposed model was applied to wind farm simulations successfully.

It is worth noting that recent developments of the AL models involve the use of non-isotropic Gaussian functions [41–43], which also aim to mimic the actual force distributions in the chordwise direction. These advanced AL models are discussed in Section 3.1.

### 2.5. Models for Nacelle and Tower

Although the nacelle and the tower have a dimension significantly smaller than the rotor, especially for a modern wind turbine of Megawatt scale, it is still critical to accurately model these auxiliary components, since they played a non-negligible role in triggering or enhancing the instability of the wake for both near wake TKE generation [44,45] and far wake evolution [46,47]. Figure 4 shows an example comparing the simulation results with/without a nacelle model. As seen, the wake meandering is less intense when the nacelle model is excluded.



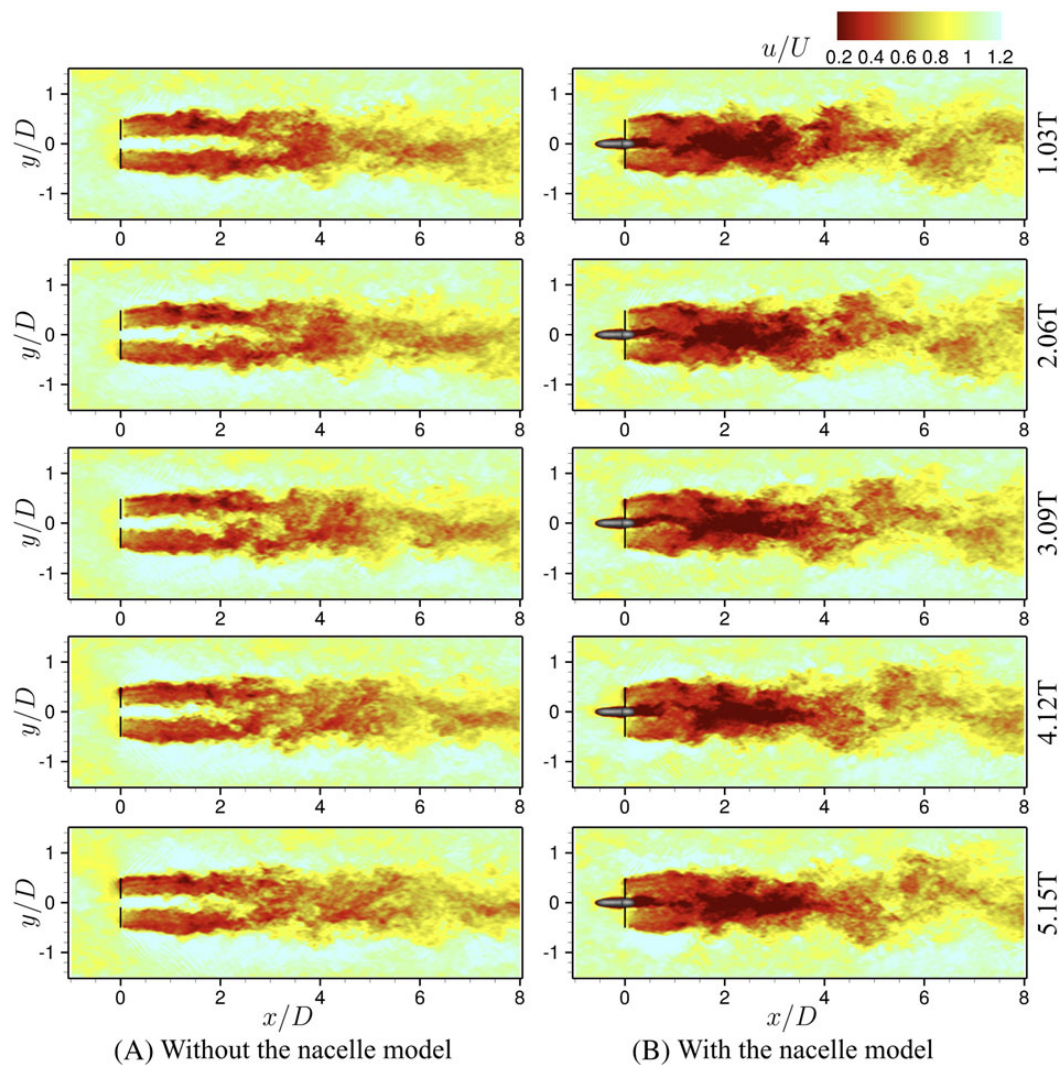


**Figure 4.** Contours of instantaneous streamwise velocity behind a hydro-kinetic turbine at different time instants without (A) and with (B) the actuator nacelle model. Reprinted with permission from Yang and Sotiropoulos [10], 2018, John Wiley and Sons.

Models of different complexity have been developed in the literature. The simplest approach is to model the nacelle and tower as drag disk and line, respectively [27]. For example, the force exerted on the nacelle is computed as,

$$F_{nacelle} = \frac{1}{2} \rho C_{D,nacelle} A_{nacelle} U_{\infty}^2 \quad (24)$$

where  $C_{D,nacelle}$  is the drag coefficient,  $A_{nacelle}$  is the projected area of the nacelle normal to the incoming flow. The drag line model for the tower is basically the same as the AL model but uses the drag coefficient of a circular cylinder.

The deficiency of the drag disk/line models is that they act similar to a porous medium, which allows the flow to pass through the body, and thus cannot accurately generate the vortex structure in its wake [48]. Taking the tower as an example, the drag line model only exerts an in-line force on the flow, without enforcing the non-penetration condition on the solid boundary. A remedy was proposed by Churchfield et al. [48], which applies the normal forces over the entire circumference of the cylinder with the force amplitude computed with the pressure coefficient  $C_p(\theta)$ . Figure 1 of Ref. [48] illustrated evidently that this more advanced approach captures the instability of the cylinder wake while the simple AL model does not.



A more sophisticated way is to model the nacelle/tower using the actuator surface concept, e.g., the actuator surface nacelle model of Yang and Sotiropoulos [10]. This model enforces the non-penetration boundary condition on the nacelle surface similar to the direct forcing immersed boundary method [49]; the tangential forces are parameterized by the friction coefficient, which is a compromise considering the relatively coarse grid employed in wind turbine wake simulations. One advantage of the AS nacelle model lies in its capability to model nacelles of arbitrary geometry [50] in different scenarios, such as yawed [51] or waked [52] wind turbines.

### 3. Advanced Topics in Wind Turbine Parameterizations

After describing the basics of wind turbine parameterization methods, we proceed to some advanced topics with different models in this section. When the wind turbine parameterization models are implemented directly as described in Section 2, the simulation results may not be satisfactory at the first attempt. For example, one common observation associated with the standard AL model is that the sectional load at the tip and root region tends to be overestimated systematically [53]. The research community has identified several reasons for this systematic error and has proposed extra corrections to the standard models. These advanced corrections are involved in (1) the force distribution function, (2) the reference velocity sampling, and (3) the tip-loss.

#### 3.1. Distribution of Actuator Forces

For wind turbine parameterization methods, the actuator forces are distributed from the grid nodes discretizing the actuator disk/line/surface to the background grid nodes for solving the flow field. This procedure is employed for two reasons, (1) the fluid and the actuator geometry are often discretized using two sets of independent grids (see Figure 5 for example), such that applying forces on the grid for the fluid is not straightforward; (2) applying the forces to the momentum equation (Equation (2)) as a concentrated source may introduce nonphysical oscillations in the flow field [18].

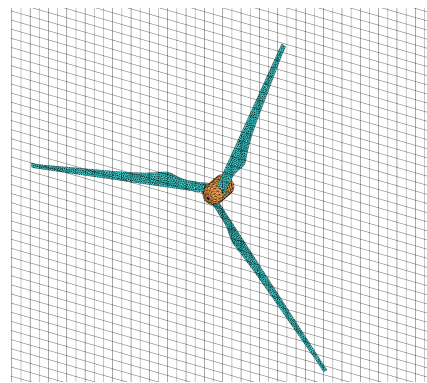


**Figure 5.** Cartesian grid discretizing the background fluid domain and triangular mesh discretizing the AS model for the rotor and the nacelle employed in VFS-Wind solver [54].

To overcome these difficulties, a regularization function (or a distribution function)  $\eta_\epsilon$  is applied on the body force  $f_i$  to distribute the load smoothly in the vicinity of the point of action  $\vec{x}'$ ,

$$f_i^\epsilon(\vec{x}) = f_i \otimes \eta_\epsilon = \iiint f_i(\vec{x}') \eta_\epsilon(\vec{x}' - \vec{x}) d\vec{x}'^3. \quad (25)$$

The force distribution  $\eta$  is often the Gaussian function [8] or its variants [55,56]. The smoothed discrete delta function [57] and piece-wise projection function [58] from the immersed boundary methods are adopted as well. Besides the above force smearing techniques, some progress toward a smearing-free actuator force has also been made [59,60] by modeling the force with a jump condition of the pressure.

### 3.1.1. Gaussian Distribution

The Gaussian distribution function in three-dimensional space can be written as follows,

$$\eta_{\varepsilon}^{3D}(\vec{r}) = \frac{1}{\varepsilon_1 \varepsilon_2 \varepsilon_3 \pi^{3/2}} \exp \left[ - \left( \frac{r_1}{\varepsilon_1} \right)^2 - \left( \frac{r_2}{\varepsilon_2} \right)^2 - \left( \frac{r_3}{\varepsilon_3} \right)^2 \right] \quad (26)$$

where  $\vec{r} = (r_1, r_2, r_3)$  denotes the distance between the grid node on the turbine and the background grid node.  $\varepsilon_i$  is a user-defined length scale for adjusting the width of the regularization function in three orthogonal directions. If the length scales in each direction are the same ( $\varepsilon_1 = \varepsilon_2 = \varepsilon_3 = \varepsilon$ ), then the Gaussian distribution is called isotropic. Otherwise, it is a non-isotropic Gaussian distribution with different widths in different directions.

Current research has revealed that both aerodynamic performance [61] and numerical stability [62] are significantly influenced by the force distribution, thus the optimal projection width should be determined from both aspects. In the following, the use of the Gaussian projection function is reviewed for different wind turbine parameterization models.

- **AD model:** The AD model often adopts the 3D isotropic Gaussian distribution for the force distribution, e.g., Sørensen et al. [20], Meyers and Meneveau [23]. Some AD models also adopt the 1D Gaussian distribution (only in the streamwise direction) [28,63]. In general, the force distribution width  $\varepsilon$  should be constrained by both rotor diameter  $D$  and grid spacing  $h$ . Sørensen et al. [20] tested the effect of  $\varepsilon$  with an isotropic 3D Gaussian distribution. Their results show that increasing  $\varepsilon$  tends to spread the force beyond the disk edge, making the apparent disk larger than its actual size, while a small  $\varepsilon$  results in a very sharp transition between the actuator disk and the freestream flow. Thereto, Sørensen and Kock [18], Mikkelsen [63] and Wu and Porté-Agel [27] suggested to set  $\varepsilon$  the same as the grid size  $h$ .
- **AL model:** Three constraints limit  $\varepsilon$  in the AL model, i.e.,  $D$ ,  $c$  (the blade chord length) and  $h$ . The first constraint, related to  $D$ , is imposed mainly to guarantee a correct rotor size for the same reason as the AD model. Martínez et al. [61] found that increasing the smearing length in the AL model also leads to an over-prediction of the turbine power. Martínez-Tossas et al. [64] suggested to use  $\varepsilon = 0.035D$  for their cases. The second constraint, imposed by the chord length  $c$ , is often more restricted than the first one since the blade is slender for modern wind turbines. From the property of the Gaussian kernel, it is suggested to use  $\varepsilon = c/4.3$  so that the force roughly spans from the leading to the trailing edge [6].

The results from the work by Martínez-Tossas et al. [65] suggested that using  $0.14c \leq \varepsilon^{\text{opt}} \leq 0.25c$  reproduces the flow around a 2D Joukowski airfoil with the best accuracy (see Figure 6). The third constraint, related to the grid size  $h$ , is imposed for stability purposes. In the study of Troldborg et al. [62], Troldborg [66], it was found that the Gaussian radius must be set  $\varepsilon > 1.5h$  to avoid spurious oscillations of the blade load and recommended  $\varepsilon = 2h$ . More restrict requirement ( $\varepsilon > 4h$ ) was also suggested [41]. With the consideration of the force distribution width, Churchfield et al. [6] derived a grid spacing of more than eight grid nodes per chord length near the blade. However, such a requirement implies a very large number of grid nodes and has to be relaxed if the focus is on the far wake evolution [67]. Jha et al. [68] proposed to use an equivalent elliptical wing, whose chord  $c^*$  naturally diminishes to zero and to determine the  $\varepsilon$  using  $c^*$  at each blade section. The authors argued that such a distribution represents better the bounded circulation on the blade. Recently, some dedicated corrections have been proposed for simulations using coarsely resolved AL models, for example, Martínez-Tossas and Meneveau [69] and Meyer Forsting et al. [70]. For non-isotropic projection, setting  $\varepsilon_c \approx \varepsilon^{\text{opt}}$  in the streamwise direction and  $\varepsilon_t \approx 0$  in the thickness direction results in a more realistic induced velocity field in the 2D airfoil test [65]. Churchfield et al. [55] demonstrated in a 3D AL simulation that the non-isotropic blade force projection results in a more realistic tip vortex, which allevi-

ates the tip load overprediction and reduces the error in the power prediction, even without applying any explicit tip-loss correction.

- **AS model:** Regarding the AS model, there has not been much discussion on the optimal force distribution. However, since the AS model already spreads the force along the chordwise direction explicitly, one can consider the AS model as a kind of AL model with an idealized chordwise force distribution.

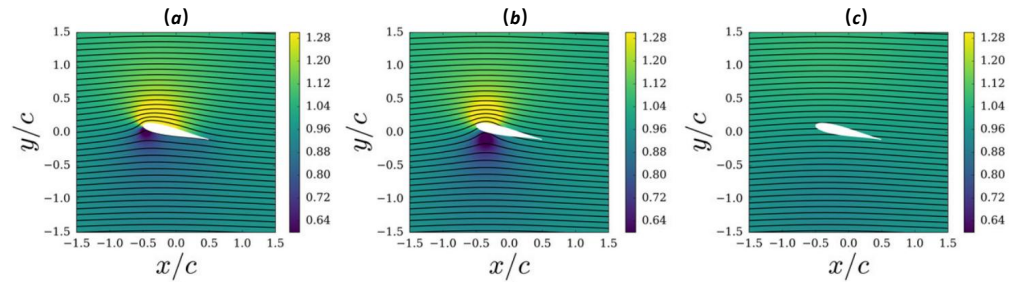


**Figure 6.** Contours of the velocity magnitude and the streamlines. (a) Potential flow solution for a symmetric Joukowski airfoil. (b) With optimal  $\epsilon = 0.14c$ . (c) With non-optimal  $\epsilon = c$ . (b,c) Based on linearized Euler equation. Reprinted with permission from Ref. [65]. 2017, John Wiley and Sons.

### 3.1.2. Discrete Delta Function

Besides selecting the proper values of  $\epsilon$ , another difficulty related to the Gaussian function is that it has to be truncated numerically in the simulation in order to ensure computational efficiency. From the computational efficiency point of view, a narrow force distribution width is beneficial, but a narrow distribution cannot guarantee the conservation of force and torque. Another approach for force distribution is to employ the discrete delta function [71,72], which conserves the force and torque in a compact stencil by satisfying certain moment conditions. The discrete delta function was firstly employed in the AD simulations of infinite large turbine arrays by Yang et al. [73]. Its applications with the AL and AS models can be found in the papers by Yang et al. [54] and Xie [58], and Yang and Sotiropoulos [10], respectively.

An example of a one-dimensional 5-point discrete function reads as follows,

$$\phi_4^*(r') = \begin{cases} \frac{3}{8} + \frac{\pi}{32} - \frac{r'^2}{4}, & |r'| \leq 0.5 \\ \frac{1}{4} + \frac{1-|r'|}{8} \sqrt{-2 + 8|r'| - 4r'^2} - \frac{1}{8} \arcsin(\sqrt{2}(|r'| - 1)), & 0.5 \leq |r'| \leq 1.5 \\ \frac{17}{16} - \frac{\pi}{64} - \frac{3|r'|}{4} + \frac{r'^2}{8} + \frac{|r'|-2}{16} \sqrt{-14 + 16|r'| - 4r'^2} \\ \quad + \frac{1}{16} \arcsin(\sqrt{2}(|r'| - 2)), & 1.5 \leq |r'| \leq 2.5 \\ 0, & 2.5 \leq |r'| \end{cases} \quad (27)$$

with  $r' = r/h$  the non-dimensional distance,  $r$  is the distance between the background grid node and the actuator grid node, and  $h$  is the spacing of the background grid. The above discrete delta function, which was developed by Yang et al. [72] using a smoothing technique from a regular 4-point piecewise discrete delta function, not only satisfies certain moment conditions itself and but also its first derivative. Validation cases show the above discrete delta function can significantly reduce the non-physical force oscillations, which were observed for conventional discrete delta functions [72]. Figure 7 compares the above mentioned discrete delta functions with the Gaussian kernel ( $\epsilon = h$ ). The numerical test of Xie [58] showed that the Gaussian function needs a wider stencil to achieve the same accuracy and stability as the 4-point piecewise function.

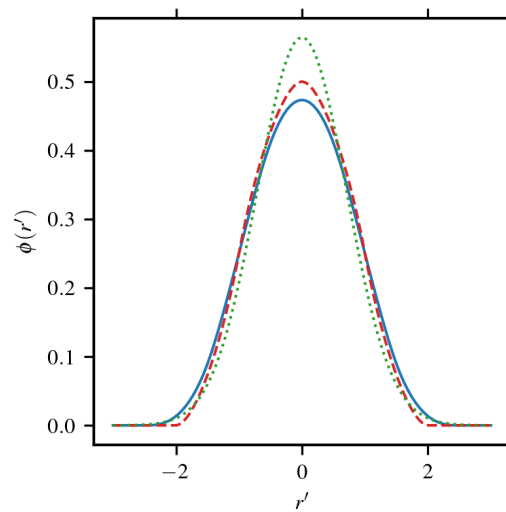


**Figure 7.** Comparison of the force projection functions: Smoothed 4-point piecewise discrete delta function (blue solid line), 4-point piecewise discrete delta function (red dashed line), and Gaussian function with  $\varepsilon = 1$  (orange dotted line).

### 3.2. Reference Velocity Sampling

Obtaining the reference velocity is another key factor for turbine parameterization models. The major difficulty lies in the complex flow physics around the rotor, which is always a mixture of the incident and the induced velocities. This scenario is different from the ideal conditions for defining the force coefficients, where the reference velocity is not influenced by the rotor [74]. Besides the complex flow physics, the accuracy in computing the reference velocity is also affected by the errors introduced by the spatial discretization scheme and the force distribution process, which should be estimated and corrected.

#### 3.2.1. Actuator Disk Model

Unless for a stand-alone wind turbine under uniform inflow, the reference velocity must be sampled from the simulated velocity field when the AD model is employed for a waked wind turbine or a wind turbine in complex terrain. One option to compute the reference velocity is to use the velocity upstream the turbine, e.g., 1D upstream in Politis et al. [75]. Another option is to use the velocity  $U_d$  averaged over the rotor disk together with a modified thrust coefficient (Equations (8) and (9)), see Meyers and Meneveau [23], Calaf et al. [24], and Yang et al. [73]. Later, Shapiro et al. [76] argued that this rotor-averaged velocity is grid-spacing dependent, and proposed to multiply the disk averaged velocity by a correction factor  $M$ , defined as follows

$$M = \left( 1 + \frac{C'_T}{2} \frac{1}{\sqrt{2\pi}} \frac{\varepsilon}{R} \right)^{-1}. \quad (28)$$

They demonstrated that the power coefficient  $C_p$  can be accurately computed on a coarse grid with  $h/D \approx 1/6$  and  $\varepsilon/D \approx 1/(2\sqrt{6})$  (N.B.: the original expression in Ref. [76] is  $\Delta/D \approx 1/2$ , where  $\Delta$  is equivalent to  $\varepsilon$  with  $\Delta = \sqrt{6}\varepsilon$ ).

#### 3.2.2. Actuator Line Model

For the AL model, the relative incoming velocity  $\mathbf{U}_{rel}$ , needs to be sampled from the simulated velocity field (Figure 2). In the definition of 2D airfoil lift and drag coefficients,  $\mathbf{U}_{rel}$  is the incoming freestream velocity, such that the velocity induced by the local loads  $L$  and  $D$  should be excluded. The velocity sampling methods can be categorized into two groups, i.e., collated sampling and non-collated sampling, determined by the location of the sampling point with respect to the actuator point.

- **Collocated single point sampling:** This option is adopted by many authors, e.g., Jha et al. [68] and Troldborg et al. [77], because the collocation sampling can exclude the induction velocity caused by the lift  $L$  at the position of the actuator point. This is because, from the idealized potential flow point of view, the effect of a concentrated lift is equivalent to a bounded circulation. For a smearing lift force using the Gaussian kernel for the distribution, this property is also proved mathematically by Martínez-Tossas et al. [65] and Meyer Forsting et al. [70]. The drag force, on the other hand, induces a non-zero velocity at the collocation point so that the sampled velocity  $\mathbf{U}_s$  is different from the relative incoming velocity  $\mathbf{U}_{rel}$ . A relation between  $\mathbf{U}_s$  and  $\mathbf{U}_{rel}$  is proposed by Martínez-Tossas et al. [65], as follows,

$$\mathbf{U}_{rel} = \frac{\mathbf{U}_s}{1 - \frac{1}{4\sqrt{\pi}} C_d \frac{\xi}{\epsilon}}, \quad (29)$$

where  $C_d$  is the drag coefficient of the airfoil.

- **Non-collocated single point sampling:** An intuitive choice is to put the velocity sampling point upstream of the actuator point to avoid local induction velocity. However, it is found by Shen et al. [78,79] that the angle of attack is much influenced by the lift induced velocity and proposed to use Biot–Savart law to correct the reference velocity. Similarly, Mittal et al. [42] employed the velocity at the grid node closest to the actuator line point as the reference velocity and also subtracted the lift induced velocity. However, it was found that the single-point sampling method results in fluctuations in the thrust and the power of the rotor.
- **Integral sampling:** To reduce the fluctuations related to the single point sampling, Churchfield et al. [55] proposed to compute  $\mathbf{U}_{rel}$  as a weighted-average in a volume close to the actuator point. In their work, the weighting function is the same Gaussian kernel as for the force distribution. The integrated sampling removes spurious high-frequency oscillations effectively. Similarly, the discrete delta function is also employed for computing the reference velocity [54]. A Lagrangian-averaged velocity sampling was proposed by Xie [58], where the reference velocity is computed as the weighted average of velocities sampled sequentially in the time, with the interval adjusted dynamically to the flow patterns to preserve the turbulence information.

### 3.2.3. Actuator Surface Model

For the AS model, the velocity sampling process is more challenging, because the blade force is distributed in a more complex manner in the chordwise direction as shown in Figure 3. In the AS model by Dobrev et al. [36], the authors proposed to sample the velocity at a point slightly upstream of the rotor to avoid the influence of the local blade but argued that this point should be sufficiently close to the rotor plane to have a correct global induced field. Alternatively, Shen et al. [9] proposed to sample the velocity at a control point located one to two chords in front of the airfoil and to correct the velocity with the induced velocity derived from the Biot–Savart law. Sibuet Watters et al. [37] and Yang and Sotiropoulos [10] employed the spatial-averaged velocity along the blade chord as the reference velocity.

### 3.3. Tip-Loss Correction

Tip-loss correction is originally employed in BEM to account for the effect of a finite number of blades, i.e., the local velocity near the blade is different from the azimuth-averaged velocity. The Glauert–Prandtl tip-loss factor derived based on the vortex theory, is the most popular one, which reads as follows,

$$F_{G-P} = \frac{2}{\pi} \arccos\left[\exp\left(-B \frac{R-r}{2r \sin \phi}\right)\right], \quad (30)$$



which is equal to the ratio of the azimuthally averaged induction factor to the local blade induction factor. Readers can refer to the work of Ramdin [80] for a detailed derivation and explanation of this formula.

For AD models, the Glauert–Prandtl tip-loss factor can be applied straightforwardly, since the same azimuthal-average assumption is employed as in the BEM [18,27]. The effect of the tip-loss correction on the rotor load was systematically investigated recently by Zhong et al. [81]. As shown in Figure 8, the over-prediction of the load near the tip region is much reduced with the tip-loss correction.

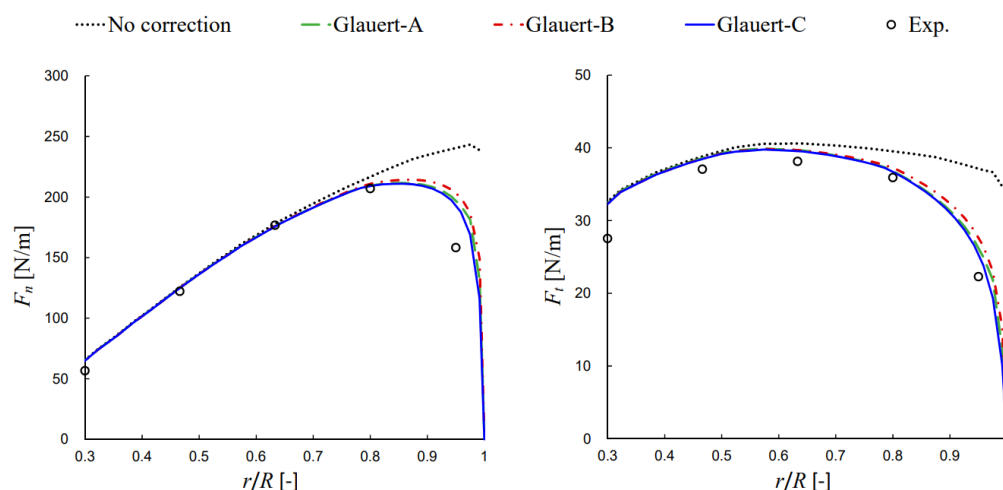


**Figure 8.** Effect of tip-loss correction on the normal ( $F_n$ ) and tangential ( $F_t$ ) forces along the NREL Phase VI blade in an AD simulation. Reprinted from Ref. [81] under Creative Commons Attribution CC BY License.

Unlike the AD model, applying Glauert–Prandtl’s tip-loss correction to the AL and AS models was argued being a controversial issue [68]. The critics argued that the tip-loss is not needed anymore since the individual blades are modeled discretely already. However, the tip-loss correction is applied in a pragmatic manner to alleviate the load over-prediction near the tip, especially when the blade is coarsely resolved [61,64].

An alternative tip-loss correction dedicated to AL simulation is then proposed by Shen et al. [33]. As opposed to Glauert–Prandtl’s tip-loss correction, Shen’s tip-loss correction is applied directly to the blade load to correct the force distribution in the blade tip region. It reads as follows,

$$F_{Sh}(r) = \frac{C_n(r)}{C_n} = \frac{C_t(r)}{C_t} = \frac{2}{\pi} \operatorname{acosexp} \left[ -g \frac{B(R-r)}{2R \sin \phi_R} \right], \quad (31)$$

where  $\phi_R$  is the angle of attack at the blade tip,  $B$  is the number of blades, and  $g$  is a coefficient to be fitted from data. A generic form of  $g$  suggested by Shen et al. [33] read as,

$$g = \exp[-c_1(B\lambda - c_2)] + 0.1, \quad (32)$$

where  $c_1$ ,  $c_2$  are adjustable coefficients to be determined from experimental data. The blade sectional forces, computed from 2D airfoil data, is multiplied by this correction factor before the projection. Shen’s tip loss correction is validated with the wind tunnel experiment of the MEXICO (Model rotor Experiment In COntrolled conditions [82,83]) project [84,85] and is later implemented in the AS model of Yang and Sotiropoulos [10].

In parallel with the above explicit and empirical tip-loss correction, recent research attributed the load over-prediction to the discretization error. It was argued that coarsely resolved tip vortex is responsible for the tip load overprediction [55,68] and the tip-loss correction is not necessary when the global induced velocity is correctly computed at the blade location [38,55]. However, fully resolving the tip vortices requires an excessive

computational cost, which hinders its direct application in farm-scale wake simulations. Further improvements on the near-tip load prediction of the AL and AS models, especially with coarse spatial resolutions, are still an active research direction. The recent results from Martínez-Tossas and Meneveau [69], Stanly et al. [86], and Meyer Forsting et al. [70] show some encouraging progresses.

#### 4. Predictive Capability of Wake Characteristics

This section is dedicated to demonstrating the predictive capability of wake characteristics of different wind turbine parameterization models, through a survey of literature on model validation against wind tunnel or field measurement, and also model-to-model comparisons. Only simple simulations are reviewed, in order to place the emphasis on the predictive capability of the wind turbine parameterization models. In this regard, the works on the effect of complex atmospheric stability conditions and complex terrains are not included. Since the wake of a wind turbine is usually split into a *near* wake and a *far* wake, the predictive capability of the above-mentioned parameterization models is analyzed separately for each region.

##### 4.1. Near Wake

The near wake starts immediately behind the rotor and extends to approximately  $2D$  to  $4D$  downstream. The flow behavior in this region depends heavily on the rotor, and serves as the starting state for the far wake evolution [5].

Several experiments focusing on the rotor load and the near wake dynamics have provided a valuable database for validating the turbine parameterization models, e.g., the EU FP5 “MEXICO” project [82], its successor project “new MEXICO” [87,88], and the blind test workshops organized by Nowitech and Norcowe [89–94]. Moreover, some experiments for the far wake evolution also record near wake features [95–97]. Besides these experimental data, the predictive capacity of the wind turbine models are also validated against the rotor resolved CFD simulation [46,53,77] or through model-to-model comparison [29,30].

- **Mean velocity:** The literature agrees that the near wake mean velocity can be predicted very well once the correct radial force distribution is applied. This is naturally achieved by the AL model and the AS model, for which the force distribution is computed from the blade information [10,53,77,98]. For the AD model, accurate near wake velocity can be predicted if the correct radial thrust distribution is provided [77,99], but the tangential force has a negligible effect on the mean streamwise velocity [30]. For an AD model with uniform force distribution, the velocity deficit has a top-hat shape [29,100,101] and persists for approximately  $2D - 3D$  downstream for simulations under turbulent inflow [57,100] and for a longer distance ( $>9D$ ) under laminar inflow condition [29]. Some special attention should also be paid to the AD model under non-uniform inflow conditions (wind shear/veer or yawed turbine), where the tangential force must be included to capture the wake asymmetry accurately [102,103]. In addition, the nacelle and the tower are critical for predicting the near wake centerline velocity, and thus should be treated properly [10,104].
- **Turbulence features:** Turbulence in the near wake is also heavily dependent on the rotor modeling. Compared with the mean velocity, the prediction of turbulence characteristics by different models is more scattered. Several factors, such as the parameterization models, the numerical discretization, the inflow turbulence, and the tower and nacelle effect, were found to affect the prediction of near-wake turbulence. Results in the literature showed that the parameterization models are prone to underestimate the turbulence intensity, e.g., when compared with the full rotor simulation in Troldborg et al. [53], and the evaluation of the AL model in the blind test workshops organized by Nowitech and Norcowe [89–94]. Such an under-prediction is related to unresolved small-scale turbulence structures within the thin shear layer dominated by the tip vortices, which are not captured by the AD model [101,105] or not fully resolved with sufficient accuracy by the AL and AS models (see the discussion fol-

lowing the next bullet). Figure 9 compares the instantaneous flow field predicted by the AL model with that of a geometry resolved simulation [43]. As for the turbulence in the hub region, Yang and Sotiropoulos [10] showed that adding a parameterization for the nacelle improves its prediction when compared with the experimental measurements [97].

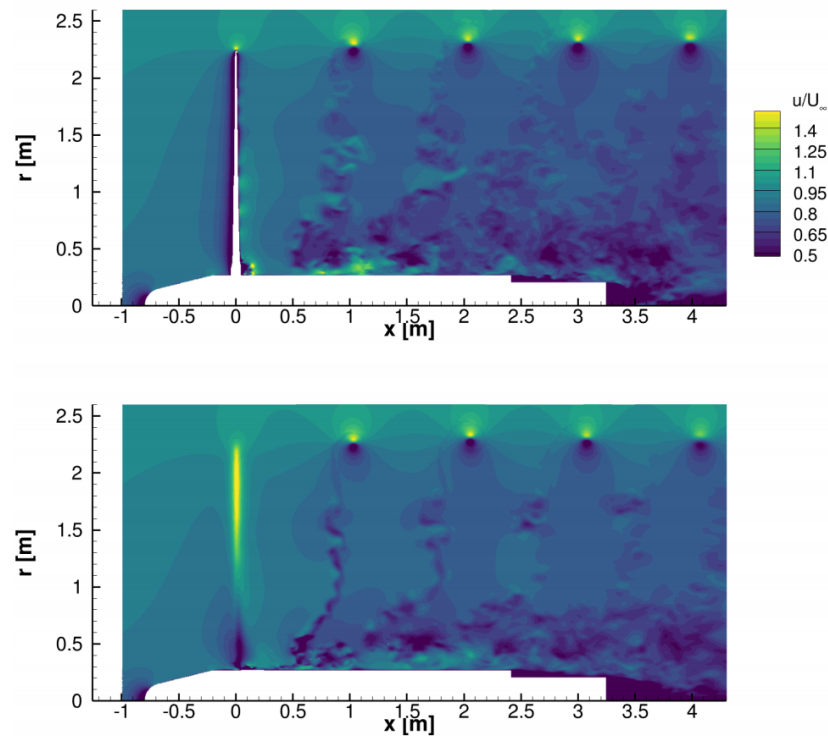


**Figure 9.** Comparison of instantaneous velocity in the blade plane. **(Top)** Geometry resolved simulation. **(Bottom)** AL simulation with anisotropic Gauss–Gumbel force distribution. Reprinted from [43] under Creative Commons Attribution 3.0 licence .

- **Tip vortex:** One important advantage of the AL and AS models over the AD model is that the tip vortices can be captured thanks to the discrete representation of the blades. The stereo PIV measurement of the near wake of the (new) MEXICO project [82,88] provides a solid database for validating the turbine parameterization models. In general, the literature agrees that the path of the tip vortex is satisfactorily captured in the simulation but the size of the vortex core is not. The simulated vortex cores are often several times larger than those in reality, as shown by Nilsson et al. [106] and Gao et al. [56] and in Figure 10. This overestimation is due to insufficient spatial resolution, although it is already refined to  $O(0.01R)$  near the tip. A later work of Nathan et al. [98], Nathan [107] also found that a coarse grid with  $h = D/32$  is sufficient to predict the mid-span velocity deficit using the AL model, but resolving the tip vortex core requires extremely fine discretization of  $h \leq D/4096$ . Similar vortex smearing is also observed in Breton et al. [108] using the AS model when comparing with the MEXICO experiment.

Albeit the challenge to predict the core size of the tip vortex, the AL model was successfully applied to study the instability of the tip vortices, e.g., Sørensen [109], Ivanell et al. [110], under simple uniform inflows. Ivanell et al. [110] studied the sensitivity of the tip vortices to ambient perturbations (Figure 11). The frequencies ( $f$ ) triggering the strongest instability are around two peaks close to  $St = fD/U_\infty = 4$  and  $St = 10$  (Original definitions were  $fR/U_\infty = 2$  and  $fR/U_\infty = 5$  in Ivanell et al. [110]). Trolldborg et al. [62] also found that increasing the tip speed ratio results in an earlier breakdown of tip vortices and transition to turbulence.

For the AS model, the predictive capacity for the tip vortices in the near wake of a utility-scale 2.5 MW wind turbine was demonstrated by Yang et al. [111], in which tip vortices with tails and counter-rotating spiral vortices intertwined with the tip vortices, which were observed in the field using the super-large-scale particle image velocimetry (SLPIV) [112], were well predicted.

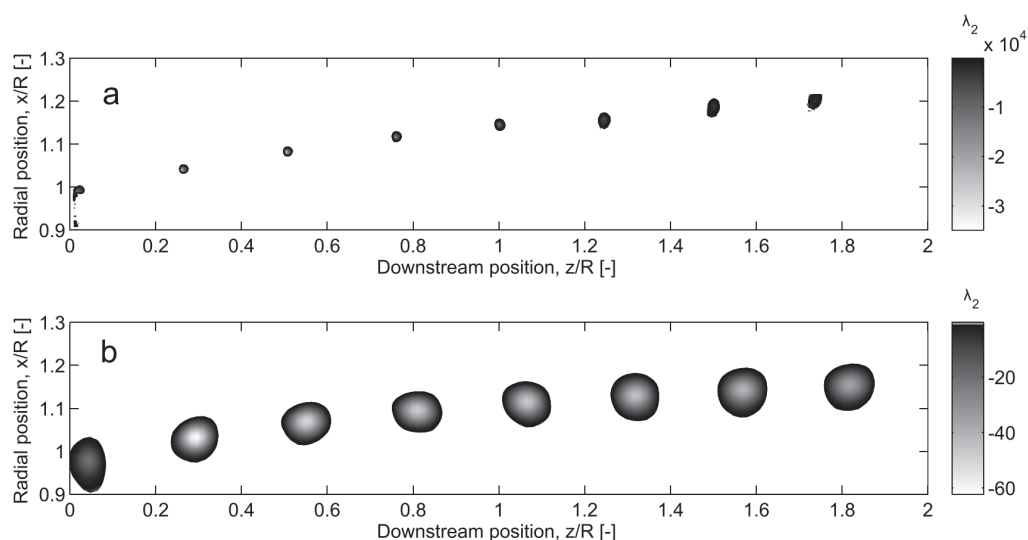


**Figure 10.** Visualization of the tip vortex cores as a function of downstream distance for  $TSR = 6.2$  for (a) the experimental measurement of the MEXICO project and (b) the AL model simulation with the grid spacing of  $h = R/122$  near the blade tip with Gaussian distribution of force. All vortices are identified with the  $\lambda_2$  criterion. Reprinted with permission from Nilsson et al. [106]. 2014, John Wiley and Sons.

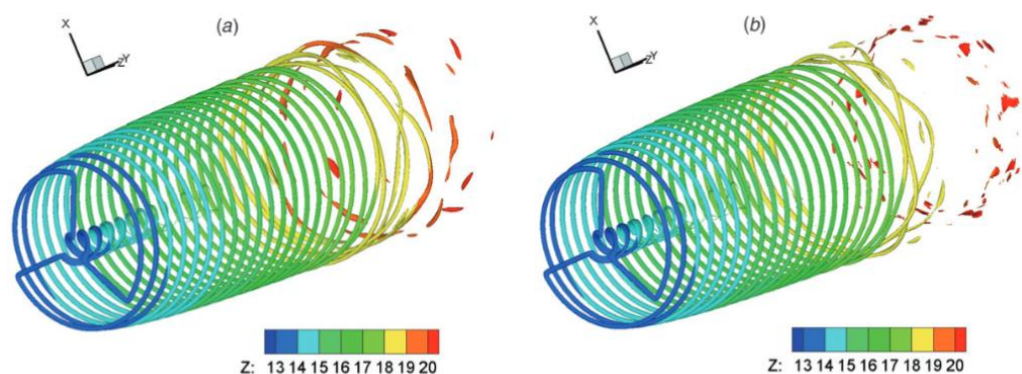


**Figure 11.** Tip vortex instability due to harmonic perturbation of blade forces of different frequencies: (a)  $fD/U_\infty = 4$  and (b)  $fD/U_\infty = 10$ . Reprinted with permission from Ivanell et al. [110]. 2010, John Wiley and Sons.

#### 4.2. Far Wake

One important goal for studying the wind turbine wake is to understand its impact on downstream rotors. In this regard, the far wake is of particular interest as turbines are separated by 7–10 rotor diameters apart in modern wind farms [113]. This section analyzes the wind turbine parameterization models in predicting the mean velocity, turbulence characteristics, and large-scale coherent structures in the wind turbine's far wake.

- **Mean velocity:** In general, the literature agrees that it is more challenging to predict the far wake for cases with low inflow turbulence. On one hand, Wang et al. [114] reported a good agreement between the AL predictions and wind tunnel measurements [114]. On the other hand, the AD and AL models are found to underestimate

the far wake diffusion compared with the full rotor prediction, even though the mean velocity in the near wake is predicted rather accurately [53]. Another interesting remark is that the AD model (with non-uniform thrust) shows the same level of accuracy when compared with the AL [53,64] and the AS models [30], promoting the use of the AD model for reducing the computational cost. For the cases under turbulent inflow, on the other hand, the mean velocity prediction becomes less dependent on the detail of the rotor so that the AL model [53,114], the AS model [10] and the AD model [100] can accurately predict the mean flow of the wake. Apart from these numerical validations, an interesting experiment investigation was conducted by Aubrun et al. [115,116] in the wind tunnel, which showed that in atmospheric boundary layer turbulence ( $TI = 0.13$ ), the wakes of a rotor and a porous disk become no longer different beyond three rotor diameters downstream. The effect of nonuniform thrust distribution and rotational force in the AD model is also found not significantly affect the far wake mean velocity (beyond  $7D$  downstream) [27,30,117] using model-to-model comparison.

- **Turbulence characteristics:** Same as for the mean wake velocity, predicting the turbulence features is also more challenging for cases with low ambient turbulence. Troldborg et al. [53] found that the wake turbulence is under-predicted by the AD and the AL models when compared with the full rotor simulation for cases with low ambient turbulence intensities. For cases with stronger inflow turbulence, the accuracy of the prediction was improved in the above-mentioned works [53,114]. This phenomenon is also supported by the experiment of Aubrun et al. [115,116]. In addition, including the rotation in the AD model is found to improve the accuracy in both uniform and turbulent inflow cases [27,30]. Martinez et al. [61] showed that a large Gaussian projection width  $\varepsilon$  can stabilize the wake shear layer and results in smaller TKE in the far wake, under uniform inflow condition.
- **Large-scale coherent structures:** The most important dynamic feature in the far wake is the low frequency, large amplitude wake meandering. These large-scale coherent structures have gained a lot of attention in wind energy research, as they are crucial for wake recovery and dynamic loads on downwind turbines [118]. A recent review on wake meandering can be found in the paper by Yang and Sotiropoulos [119]. Hence, it is important to verify how well these coherent structures can be predicted by the turbine parameterization models. Kang et al. [46] compared the predictions from the AL and AD models with those from the geometry-resolved simulations and found that both models underpredict the turbulence kinetic energy and the wake meandering. Yang and Sotiropoulos [10] showed that using the AS models for blades and nacelle can accurately predict the wake meandering, when compared with the measurements. Compared with the AS/AL models, the spatial and temporal resolutions are lower for the AD model. For simulations of wind farms with large spatial and temporal scales, the AD model is preferred because of its computational efficiency. It is important to systematically evaluate the capability of the AD model in predicting large-scale coherent structures. Li and Yang [29] analyzed the coherent structures in the wake predicted by the AD model (uniform thrust) by comparing its predictions with the AS model. The dynamic mode decomposition (DMD) analyses reveal distinct coherent structures for the wake predicted by the AD model and the AS model in terms of both the dominant frequencies and spatial patterns of different DMD modes as shown in Figure 12 for the case under uniform inflow.

In a recent work by Dong et al. [30], it was found that the capability of the AD model in predicting the turbulence kinetic energy in the far wake depends on turbine designs. For a rotor with a relatively uniform axial force coefficient, the turbulence kinetic energy predicted by the AD model is similar to those predicted by the AS model. When the axial force coefficient has a strong radial variation, i.e., lower near the tip but higher near the root, the wake meandering is underpredicted by the AD model



than the AS model does, also resulting in lower turbulence kinetic energy for the AD model prediction.

The wind turbine parameterization models were successfully applied to study the mechanism of wake meandering. For instance, the far wake meandering triggered by the shear layer instability of the wake was investigated by Mao and Sørensen [120] using the AD model and Gupta and Wan [121] using the AL model. For a floating offshore wind turbine, Li et al. [50] found that small-amplitude turbine's side-to-side motion ( $\sim 0.01D$ ) of certain frequencies ( $0.2 < St < 0.6$ ) can trigger far wake meandering of high amplitude ( $\sim D$ ), by using the AS simulations. Moreover, Li et al. [50] also showed that both uniform and non-uniform AD models with the AS nacelle model are able to capture such instability. Using the AS simulations, Yang and Sotiropoulos [122] showed the co-existence of the inflow large eddy mechanism and the shear layer instability mechanism for wake meandering.

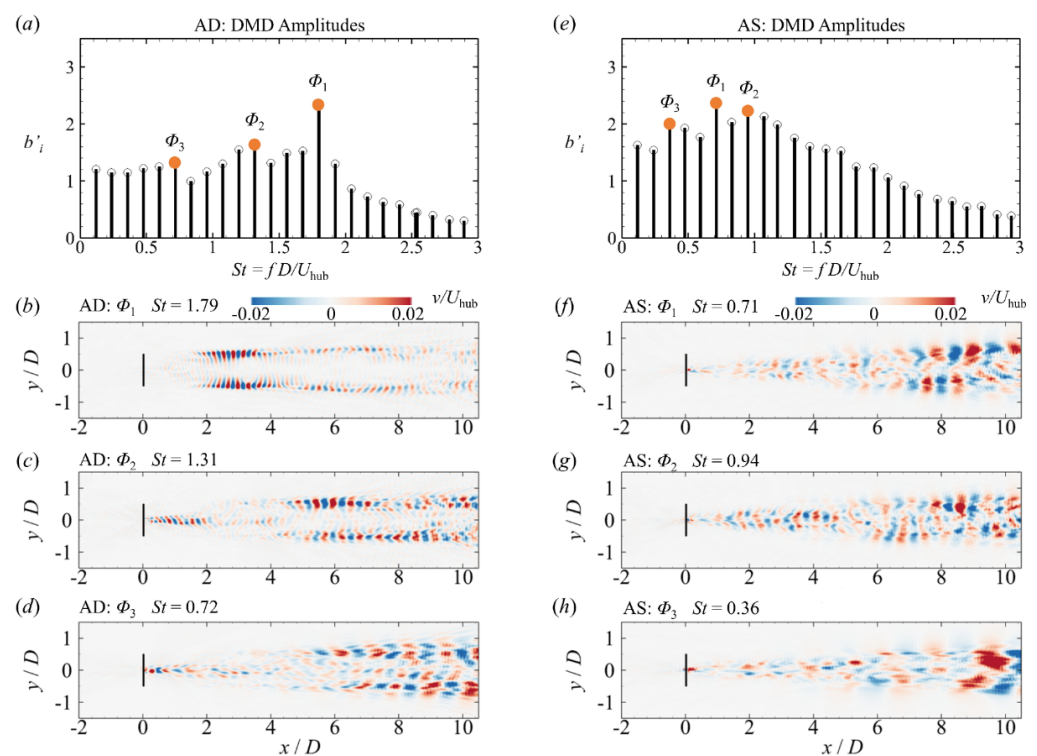


**Figure 12.** Coherent structure in the wake revealed by dynamic mode decomposition (DMD) behind an AD modeled (left column) and an AS modeled wind turbine (right column). (a,e) The eigenvalue-weighted amplitudes of the DMD modes; (b–d) the first three principal modes predicted by the AD model; (f–h) the first three principal modes predicted by the AS model. Reprinted from Ref. [29] under Creative Commons Attribution License.

## 5. Applications to Utility-Scale Wind Farms

This section showcases the applications of wind turbine parameterization models to utility-scale wind farms.

Horns Rev is probably the most well-known wind farm. Different wind turbine parameterization methods have been employed to simulate the flow through Horns Rev wind farm. For instance, Porté-Agel et al. [123] employed an AD model with rotation in their simulation, with a coarse grid spacing  $O(D/5)$ . The power derived from the AD model [124] shows a good agreement with the observation. Using the AS models for both rotor and nacelle, Foti et al. [40] simulated the flow inside Horns Rev wind farm to investigate the effects of the nacelle on wake meandering. A grid spacing of  $h \approx 2$  m, ( $O(D/40)$ ) is employed, with a total of 340 million grids. The simulation reveals that the wake meandering amplitudes are underpredicted if the nacelle is not modeled. Joulin

et al. [125] simulated the flow inside the Horns Rev wind farm using the open-source non-hydrostatic mesoscale atmospheric model Meso-NH with the AL model, which considers the thermal exchanges, humidity, cloud formation, and precipitation. Figure 13 shows the visualization of the cloud mixing ratio from their simulation, showing an impressive agreement with the photo.

Other offshore wind farms have also been simulated in the literature [6,126–129]. For example, Churchfield et al. [6] investigated the turbulence flow of Lillgrund offshore wind plant. The simulation covers an area of  $4 \text{ km} \times 4 \text{ km}$  with 48 Siemens wind turbines ( $D \approx 93 \text{ m}$ ). The AL model was adopted instead of the AD model since the spacing between wind turbines is rather small ( $3D \sim 4D$ ) requiring a better prediction of the near wake. The simulation is conducted with OpenFOAM [130] with 315 million cells at a spatial resolution  $O(1\text{m})$  near the blade and  $O(10\text{m})$  in the far-field.

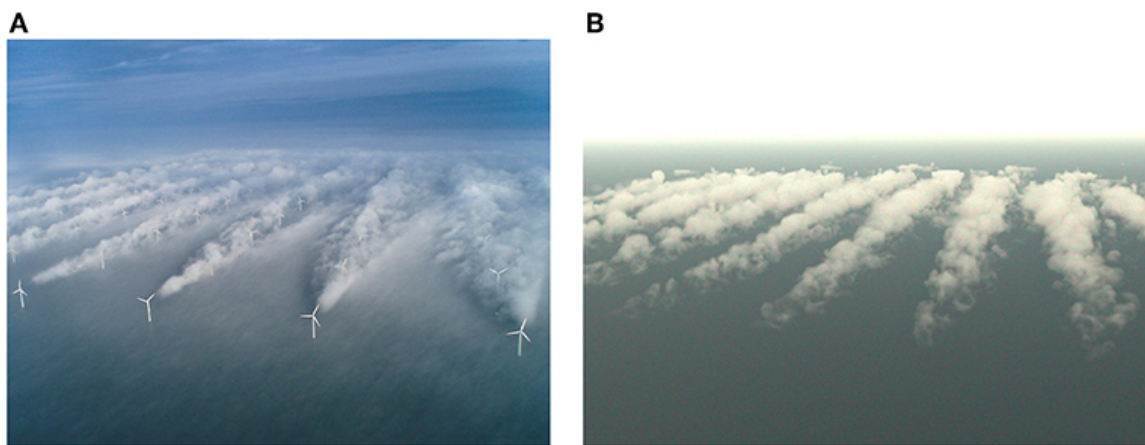


**Figure 13.** (A) Photograph of the wake of Horns Rev 1 wind farm (Courtesy: Vattenfall. Photographer is Christian Steiness). Reprinted from [131] under Creative Commons Attribution License. (B) Post-processing of the simulated cloud mixing ratio with a rendering algorithm. Reprinted from Joulin et al. [125] under Creative Commons Attribution License.

Simulations of wind farms over complex terrain were also carried out in the literature [132,133]. Yang et al. [132] simulated the flow over a wind farm in complex terrain using the AL model. The sizes of the computational domain are approximately  $12 \text{ km} \times 4 \text{ km} \times 1 \text{ km}$ , with the grid spacing at  $O(3 \text{ m})$  in the vertical direction and  $O(10 \text{ m})$  in the horizontal directions. Since it is challenging to generate turbulent inflows for complex terrains, Yang et al. [132] employed a buffer region to feed at the inlet the fully developed turbulent flows from a precursory simulation for flat terrain. The computed power outputs are in good agreement with those from the measurements as shown in Figure 14. The effects of an idealized two-dimensional hill on wind farms are systematically investigated by Liu and Stevens [133] by using LES with the filtered AD model [76] for the turbines and the immersed boundary method for the hill. It is found that turbines taller than the hill can benefit from the terrain effect, while turbines shorter than the hill will produce much less power if they are located on the downwind side of the hill.

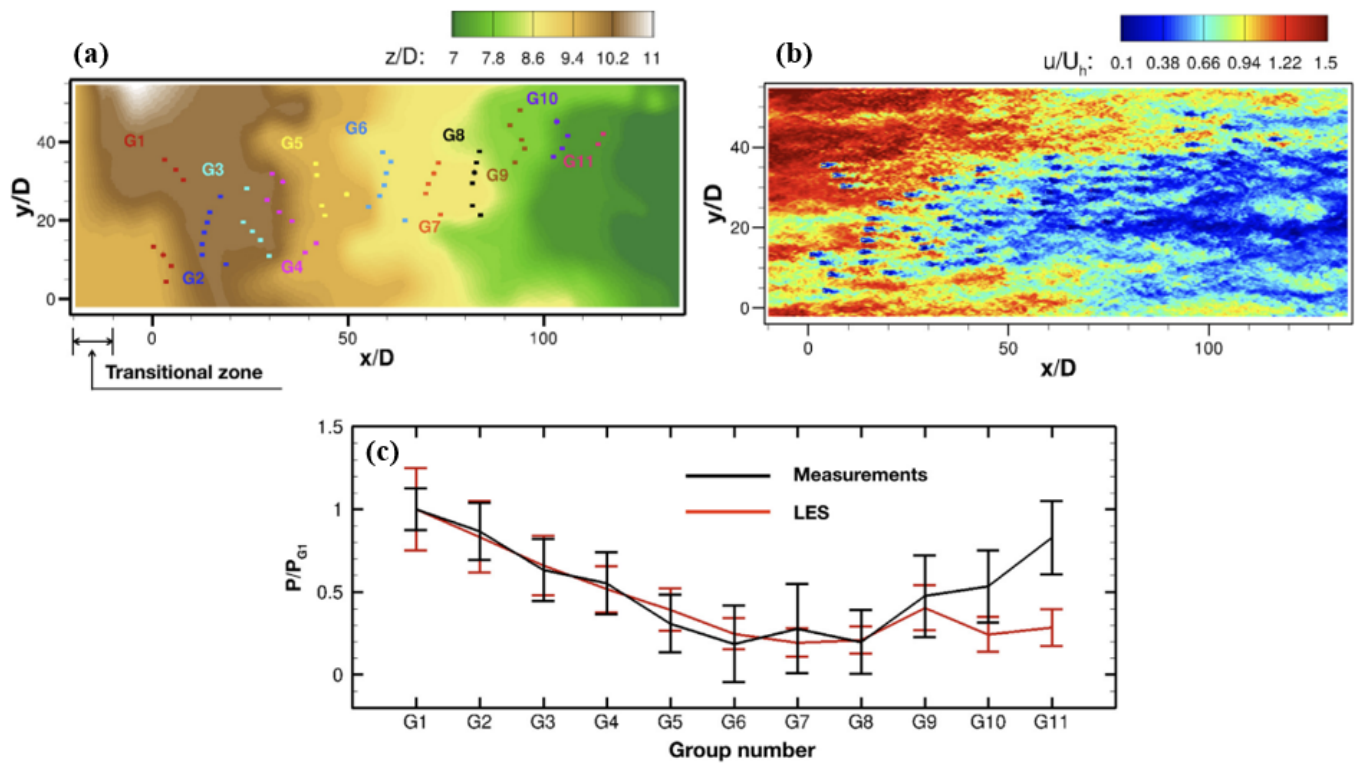


**Figure 14.** Results from the AL-LES simulation of the flow inside a wind farm over complex terrain for (a) contour of the terrain elevation, (b) instantaneous downwind velocity, and (c) comparison of the simulated power outputs with measurements. Reprinted from Yang et al. [132] with permission, 2018, Elsevier.

Understanding the farm–farm interaction is also important for planning and operating a farm in an area clustering several wind farms [134–137]. Dong et al. [138] applied the AD model to investigate the wake of an idealized wind farm consisting of 40 wind turbines ( $D = 100$  m). The spatial resolutions  $O(2$  m) in the vertical direction and  $O(10$  m) in the horizontal directions, resulting in a total of 254 million grid nodes. The simulation results show that the velocity deficit of the wind farm wake recovers 95% at 5.5 km downstream and persists for more than 16.5 km from the last row as shown in Figure 15. Eriksson et al. [134] compared the prediction capability of AD+LES (EllipSys3D) with wind farm parameterization (WFP) + weather research and forecasting (WRF) using the field measurement of Lillgrund wind farm. The computational domain for the LES extends until 7 km behind the wind farm and the spatial resolution for the LES is  $O(D/20)$ , making a total number of 400 million grid nodes. The WRF simulation of the same site employed a grid resolution of approximately  $O(1D)$ . Wind farm production data agrees better with the LES prediction, while the results of WRF clearly overestimated the production due to the coarse resolution and the uncertainty due to the higher level simplification of the WFP. The detailed wake dynamics provided by the LES can thus provide insights into the complex fluid dynamics of the far wake evolution behind wind farms and is useful for further improving the WFP in WRF.



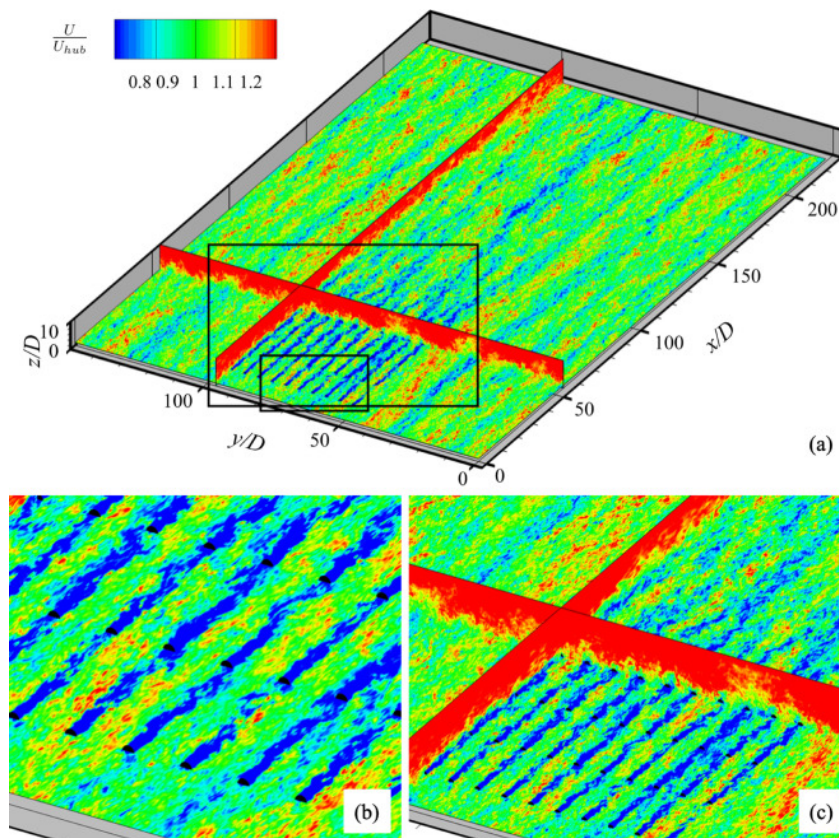


**Figure 15.** A simulation of wind farm wake by using AD-LES. (a) contours of the instantaneous streamwise velocity at hub height; (b,c) zoomed-in contours. Reprinted from Dong et al. [138] under Creative Commons Attribution License.

## 6. Summary

This paper reviewed the existing wind turbine parameterization models, i.e., the actuator disk (AD) model, the actuator line (AL) model, and the actuator surface (AS) model for large-eddy simulation of wind turbine wakes.

The fundamentals for each parameterization model were described. A special focus was on some advanced numerical issues with the parameterization models, including the methods for force projection and velocity sampling, and tip loss correction. The influences of these parameters are shown on the predicted wind turbine load and power. The Gaussian function is often employed for force distribution. The discrete delta function distributing the force in a compact way is suggested for a relatively lower computational cost. Different approaches for velocity sampling were employed in the literature. For the AD model, it can be some diameters upstream of the rotor. For the AL model, it often co-locates with the AL, or locates at some distances upstream of the AL. For the AS model, it can co-locate with the leading edge, or locates at some distances upstream of the leading edge. As for the tip correction, although some works suggest that it can be removed in the AL/AS model when the tip vortices are fully resolved, it is still suggested to use the tip loss correction in the AL/AS simulations in order to accurately predict the load using a coarse grid. The recent development of the AL model is to employ a non-isotropic force distribution, taking into account the realistic blade geometry, which will eventually make the AL model equivalent to the AS model. Besides the rotor, the literature also suggests that properly modeling the nacelle and the tower either using the immersed boundary method [45] or an actuator surface model [10] is important for accurately predicting the near wake dynamics and the meandering of the far wake.

The review of the validations of different parameterization models shows that these wind turbine parameterization models provide different levels of predictive capacity at

different computational costs. The selection of a specific parameterization model is a compromise between the accuracy, the computational cost, and the scale of the problem. The high computational cost of the AL/AS models not only lies in the required high spatial resolutions but also in the small time steps related to the limit set by the tangential velocity of the blade tip. For a stand-alone wind turbine case, the computational cost is low for any parameterization models. For utility-scale wind farms, the AD model is preferred, although the AS model has been employed to simulate the Horns Rev wind farm at a much higher computational cost [40]. The predictive capability for the AD model was observed to vary for different inflows. The wake is better predicted for cases with turbulent inflows than for cases with uniform inflow [29]. Interestingly, such a difference in predictive capability was also observed for different wind turbine designs [30]. Taking into account the rotational effect and the radial distribution of the forces in the AD model was found to be able to improve its prediction accuracy, especially in the near wake.

At last, applications of the parameterization models to simulations of utility-scale wind farms were briefly reviewed, with no intention to include all related works. The literature review showed that the wake effects are still noticeable even several kilometers downstream. Further studies on turbulent flows over wind farms to investigate farm–farm interactions and their effects on mesoscale meteorology are certainly needed with the fast growth of wind power globally.

Recently, data-driven models have emerged in wind energy research and are expected to play an increasingly important role [139]. Large-eddy simulations incorporating wind turbine parametric models provide a feasible way to generate the database for training these data-driven models. For example, the data generated by the AS model were employed by Yang [140] to train a neural network model to predict the instantaneous wake centers. The data-driven wind turbine wake model of Wang et al. [141] was developed based on a database generated with the actuator disk model with rotation (AD-R). The reduced-order model developed by Iungo et al. [142] to predict the instantaneous flow field partially utilized the data from the AL simulations. Apparently, the accuracy of these data-driven models is directly dependent on the accuracy of the turbine parameterizations, which must be carefully selected according to their predictive capability to ensure that the wake characteristics of concern are captured.

**Author Contributions:** Conceptualization, Z.L. and X.Y.; investigation, Z.L.; resources, X.Y.; writing—original draft preparation, Z.L. and X.L.; writing—review and editing, Z.L., X.L., and X.Y.; supervision, X.Y.; project administration, X.Y.; funding acquisition, X.Y. All authors have read and agreed to the published version of the manuscript.

**Funding:** This work was funded by the NSFC Basic Science Center Program for “Multiscale Problems in Nonlinear Mechanics” (NO. 11988102), National Natural Science Foundation of China (NO. 12172360).

**Institutional Review Board Statement:** Not applicable.

**Informed Consent Statement:** Not applicable.

**Data Availability Statement:** Not applicable.

**Conflicts of Interest:** The authors declare no conflict of interest.

## References

1. Barthelmie, R.J.; Hansen, K.S.; Frandsen, S.T.; Rathmann, O.; Schepers, J.G.; Schlez, W.; Phillips, J.; Rados, K.; Zervos, A.; Politis, E.S.; et al. Modelling and measuring flow and wind turbine wakes in large wind farms offshore. *Wind Energy* **2009**, *12*, 431–444. [[CrossRef](#)]
2. Thomsen, K.; Sørensen, P. Fatigue loads for wind turbines operating in wakes. *J. Wind Eng. Ind. Aerodyn.* **1999**, *80*, 121–136. [[CrossRef](#)]
3. Stevens, R.; Meneveau, C. Flow structure and turbulence in wind farms. *Annu. Rev. Fluid Mech.* **2017**, *49*, 311–339. [[CrossRef](#)]
4. Porté-Agel, F.; Bastankhah, M.; Shamsoddin, S. Wind-turbine and wind-farm flows: A review. *Bound.-Layer Meteorol.* **2020**, *174*, 1–59. [[CrossRef](#)] [[PubMed](#)]



5. Sanderse, B.; Van der Pijl, S.; Koren, B. Review of computational fluid dynamics for wind turbine wake aerodynamics. *Wind Energy* **2011**, *14*, 799–819. [[CrossRef](#)]
6. Churchfield, M.; Lee, S.; Moriarty, P.; Martinez, L.; Leonardi, S.; Vijayakumar, G.; Brasseur, J. A large-eddy simulation of wind-plant aerodynamics. In Proceedings of the 50th AIAA Aerospace Sciences Meeting Including the New Horizons Forum and Aerospace Exposition, Nashville, TN, USA, 9–12 January 2012; p. 537.
7. Batten, W.M.; Harrison, M.; Bahaj, A. Accuracy of the actuator disc-RANS approach for predicting the performance and wake of tidal turbines. *Philos. Trans. R. Soc. A Math. Phys. Eng. Sci.* **2013**, *371*, 20120293. [[CrossRef](#)]
8. Sørensen, J.N.; Shen, W.Z. Numerical modeling of wind turbine wakes. *J. Fluids Eng. Trans. ASME* **2002**, *124*, 393–399. [[CrossRef](#)]
9. Shen, W.Z.; Zhang, J.H.; Sørensen, J.N. The actuator surface model: A new Navier–Stokes based model for rotor computations. *J. Sol. Energy Eng.* **2009**, *131*. [[CrossRef](#)]
10. Yang, X.; Sotiropoulos, F. A new class of actuator surface models for wind turbines. *Wind Energy* **2018**, *21*, 285–302. [[CrossRef](#)]
11. Germano, M.; Piomelli, U.; Moin, P.; Cabot, W.H. A dynamic subgrid-scale eddy viscosity model. *Phys. Fluids A Fluid Dyn.* **1991**, *3*, 1760–1765. [[CrossRef](#)]
12. Froude, R.E. On the part played in propulsion by differences of fluid pressure. In *TRANSACTIONS of the Institution of Naval Architects*; Institution of Naval Architects: London, UK, 1889; Volume 30, pp. 390–405.
13. Betz, A. Das Maximum der theoretisch möglichen Ausnutzung des Windes durch Windmotoren. *Z. Gesamte Turbinenwesen* **1920**, *20*, 307–309.
14. Betz, A. The maximum of the theoretically possible exploitation of wind by means of a wind motor. *Wind Eng.* **2013**, *37*, 441–446. [[CrossRef](#)]
15. Glauert, H. *The Analysis of Experimental Results in the Windmill Brake and Vortex Ring States of an Airscrew*; HM Stationery Office: Richmond, UK, 1926.
16. Conway, J.T. Analytical solutions for the actuator disk with variable radial distribution of load. *J. Fluid Mech.* **1995**, *297*, 327–355. [[CrossRef](#)]
17. Conway, J.T. Exact actuator disk solutions for non-uniform heavy loading and slipstream contraction. *J. Fluid Mech.* **1998**, *365*, 235–267. [[CrossRef](#)]
18. Sørensen, J.N.; Kock, C.W. A model for unsteady rotor aerodynamics. *J. Wind Eng. Ind. Aerodyn.* **1995**, *58*, 259–275. [[CrossRef](#)]
19. Sørensen, J.N.; Myken, A. Unsteady actuator disc model for horizontal axis wind turbines. *J. Wind Eng. Ind. Aerodyn.* **1992**, *39*, 139–149. [[CrossRef](#)]
20. Sørensen, J.; Shen, W.; Munduate, X. Analysis of wake states by a full-field actuator disc model. *Wind Energy: Int. J. Prog. Appl. Wind Power Convers. Technol.* **1998**, *1*, 73–88. [[CrossRef](#)]
21. Ammara, I.; Leclerc, C.; Masson, C. A viscous three-dimensional differential/actuator-disk method for the aerodynamic analysis of wind farms. *J. Sol. Energy Eng.* **2002**, *124*, 345–356. [[CrossRef](#)]
22. Jimenez, A.; Crespo, A.; Migoya, E.; Garcia, J. Advances in large-eddy simulation of a wind turbine wake. *J. Phys. Conf. Ser.* **2007**, *75*, 012041. [[CrossRef](#)]
23. Meyers, J.; Meneveau, C. Large eddy simulations of large wind-turbine arrays in the atmospheric boundary layer. In Proceedings of the 48th AIAA Aerospace Sciences Meeting Including the New Horizons Forum and Aerospace Exposition, Orlando, FL, USA, 4–7 January 2010; p. 827.
24. Calaf, M.; Meneveau, C.; Meyers, J. Large eddy simulation study of fully developed wind-turbine array boundary layers. *Phys. Fluids* **2010**, *22*, 015110. [[CrossRef](#)]
25. Calaf, M.; Parlange, M.B.; Meneveau, C. Large eddy simulation study of scalar transport in fully developed wind-turbine array boundary layers. *Phys. Fluids* **2011**, *23*, 126603. [[CrossRef](#)]
26. Glauert, H. Airplane propellers. In *Aerodynamic Theory*; Springer: Berlin/Heidelberg, Germany, 1935; pp. 169–360.
27. Wu, Y.T.; Porté-Agel, F. Large-Eddy Simulation of Wind-Turbine Wakes: Evaluation of Turbine Parametrisations. *Bound.-Layer Meteorol.* **2011**, *138*, 345–366. [[CrossRef](#)]
28. Sørensen, J.N.; Nilsson, K.; Ivanell, S.; Asmuth, H.; Mikkelsen, R.F. Analytical body forces in numerical actuator disc model of wind turbines. *Renew. Energy* **2020**, *147*, 2259–2271. [[CrossRef](#)]
29. Li, Z.; Yang, X. Evaluation of actuator disk model relative to actuator surface model for predicting utility-scale wind turbine wakes. *Energies* **2020**, *13*, 3574. [[CrossRef](#)]
30. Dong, G.; Li, Z.; Qin, J.; Yang, X. Predictive capability of actuator disk models for wakes of different wind turbine designs. *Renew. Energy* **2022**, *188*, 269–281. [[CrossRef](#)]
31. Froude, W. The Elementary Relation between Pitch, Slip, and Propulsive Efficiency. In *TRANSACTIONS of the Institution of Naval Architects*; Institution of Naval Architects: London, UK, 1878; Volume 19, pp. 22–33.
32. Schreck, S.; Robinson, M. Rotational augmentation of horizontal axis wind turbine blade aerodynamic response. *Wind Energy Int. J. Prog. Appl. Wind Power Convers. Technol.* **2002**, *5*, 133–150.
33. Shen, W.Z.; Mikkelsen, R.; Sørensen, J.N.; Bak, C. Tip loss corrections for wind turbine computations. *Wind Energy* **2005**, *8*, 457–475. [[CrossRef](#)]
34. Du, Z.; Selig, M. A 3-D stall-delay model for horizontal axis wind turbine performance prediction. In Proceedings of the 1998 ASME Wind Energy Symposium, Reno, NV, USA, 12–15 January 1998; p. 21.

35. Chaviaropoulos, P.; Hansen, M.O. Investigating three-dimensional and rotational effects on wind turbine blades by means of a quasi-3D Navier-Stokes solver. *J. Fluids Eng.* **2000**, *122*, 330–336. [[CrossRef](#)]
36. Dobrev, I.; Massouh, F.; Rapin, M. Actuator surface hybrid model. *J. Phys. Conf. Ser.* **2007**, *75*, 012019. [[CrossRef](#)]
37. Sibuet Watters, C.; Breton, S.P.; Masson, C. Application of the actuator surface concept to wind turbine rotor aerodynamics. *Wind Energy* **2010**, *13*, 433–447. [[CrossRef](#)]
38. Kim, T.; Oh, S.; Yee, K. Improved actuator surface method for wind turbine application. *Renew. Energy* **2015**, *76*, 16–26. [[CrossRef](#)]
39. Shen, W.Z.; Sørensen, J.N.; Zhang, J. Actuator surface model for wind turbine flow computations. In Proceedings of the European Wind Energy Conference and Exhibition, Milan, Italy, 7–10 May 2007; Volume 7.
40. Foti, D.; Yang, X.; Shen, L.; Sotiropoulos, F. Effect of wind turbine nacelle on turbine wake dynamics in large wind farms. *J. Fluid Mech.* **2019**, *869*, 1–26. [[CrossRef](#)]
41. Shives, M.; Crawford, C. Mesh and load distribution requirements for actuator line CFD simulations. *Wind Energy* **2013**, *16*, 1183–1196. [[CrossRef](#)]
42. Mittal, A.; Sreenivas, K.; Taylor, L.K.; Hereth, L. Improvements to the actuator line modeling for wind turbines. In Proceedings of the 33rd Wind Energy Symposium, Kissimmee, FL, USA, 5–9 January 2015; p. 0216.
43. Cormier, M.; Weihing, P.; Lutz, T. Evaluation of the Effects of Actuator Line Force Smearing on Wind Turbines Near-Wake Development. *J. Phys. Conf. Ser.* **2021**, *1934*, 012013. [[CrossRef](#)]
44. Abraham, A.; Dasari, T.; Hong, J. Effect of turbine nacelle and tower on the near wake of a utility-scale wind turbine. *J. Wind Eng. Ind. Aerodyn.* **2019**, *193*, 103981. [[CrossRef](#)]
45. Santoni, C.; Carrasquillo, K.; Arenas-Navarro, I.; Leonardi, S. Effect of tower and nacelle on the flow past a wind turbine. *Wind Energy* **2017**, *20*, 1927–1939. [[CrossRef](#)]
46. Kang, S.; Yang, X.; Sotiropoulos, F. On the onset of wake meandering for an axial flow turbine in a turbulent open channel flow. *J. Fluid Mech.* **2014**, *744*, 376–403. [[CrossRef](#)]
47. Foti, D.; Yang, X.; Guala, M.; Sotiropoulos, F. Wake meandering statistics of a model wind turbine: Insights gained by large eddy simulations. *Phys. Rev. Fluids* **2016**, *1*, 044407. [[CrossRef](#)]
48. Churchfield, M.J.; Lee, S.; Schmitz, S.; Wang, Z. Modeling wind turbine tower and nacelle effects within an actuator line model. In Proceedings of the 33rd Wind Energy Symposium, Kissimmee, FL, USA, 5–9 January 2015; p. 0214.
49. Sotiropoulos, F.; Yang, X. Immersed boundary methods for simulating fluid–structure interaction. *Prog. Aerosp. Sci.* **2014**, *65*, 1–21. [[CrossRef](#)]
50. Li, Z.; Dong, G.; Yang, X. Onset of wake meandering for a floating offshore wind turbine under side-to-side motion. *J. Fluid Mech.* **2022**, *934*, A29. [[CrossRef](#)]
51. Li, Z.; Yang, X. Large-eddy simulation on the similarity between wakes of wind turbines with different yaw angles. *J. Fluid Mech.* **2021**, *921*, A11. [[CrossRef](#)]
52. Liu, X.; Li, Z.; Yang, X.; Xu, D.; Kang, S.; Khosronejad, A. Large-Eddy Simulation of Wakes of Waked Wind Turbines. *Energies* **2022**, *15*, 2899. [[CrossRef](#)]
53. Troldborg, N.; Zahle, F.; Réthoré, P.E.; Sørensen, N. Comparison of the wake of different types of wind turbine CFD models. In Proceedings of the 50th AIAA Aerospace Sciences Meeting including the New Horizons Forum and Aerospace Exposition, Nashville, TN, USA, 9–12 January 2012; p. 237.
54. Yang, X.; Sotiropoulos, F.; Conzemius, R.J.; Wachtler, J.N.; Strong, M.B. Large-eddy simulation of turbulent flow past wind turbines/farms: The Virtual Wind Simulator (VWiS). *Wind Energy* **2015**, *18*, 2025–2045. [[CrossRef](#)]
55. Churchfield, M.J.; Schreck, S.J.; Martinez, L.A.; Meneveau, C.; Spalart, P.R. An advanced actuator line method for wind energy applications and beyond. In Proceedings of the 35th Wind Energy Symposium, Grapevine, TX, USA, 9–13 January 2017; p. 1998.
56. Gao, Z.; Li, Y.; Wang, T.; Ke, S.; Li, D. Recent improvements of actuator line-large-eddy simulation method for wind turbine wakes. *Appl. Math. Mech.* **2021**, *42*, 511–526. [[CrossRef](#)]
57. Yang, X.; Sotiropoulos, F. On the predictive capabilities of LES-actuator disk model in simulating turbulence past wind turbines and farms. In Proceedings of the 2013 American Control Conference, Washington, DC, USA, 17–19 June 2013; pp. 2878–2883.
58. Xie, S. An actuator-line model with Lagrangian-averaged velocity sampling and piecewise projection for wind turbine simulations. *Wind Energy* **2021**, *24*, 1095–1106. [[CrossRef](#)]
59. Réthoré, P.E.; Sørensen, N.N. A discrete force allocation algorithm for modelling wind turbines in computational fluid dynamics. *Wind Energy* **2012**, *15*, 915–926. [[CrossRef](#)]
60. Troldborg, N.; Sørensen, N.N.; Réthoré, P.E.; van der Laan, M. A consistent method for finite volume discretization of body forces on collocated grids applied to flow through an actuator disk. *Comput. Fluids* **2015**, *119*, 197–203. [[CrossRef](#)]
61. Martinez, L.; Leonardi, S.; Churchfield, M.; Moriarty, P. A comparison of actuator disk and actuator line wind turbine models and best practices for their use. In Proceedings of the 50th AIAA Aerospace Sciences Meeting including the New Horizons Forum and Aerospace Exposition, Nashville, TN, USA, 9–12 January 2012; p. 900.
62. Troldborg, N.; Sørensen, J.N.; Mikkelsen, R. Numerical simulations of wake characteristics of a wind turbine in uniform inflow. *Wind Energy* **2010**, *13*, 86–99. [[CrossRef](#)]
63. Mikkelsen, R. Actuator Disc Methods Applied to Wind Turbines. Ph.D. Thesis, Technical University of Denmark, Lyngby, Denmark, 2003.

64. Martínez-Tossas, L.A.; Churchfield, M.J.; Leonardi, S. Large eddy simulations of the flow past wind turbines: Actuator line and disk modeling. *Wind Energy* **2015**, *18*, 1047–1060. [[CrossRef](#)]
65. Martínez-Tossas, L.A.; Churchfield, M.J.; Meneveau, C. Optimal smoothing length scale for actuator line models of wind turbine blades based on Gaussian body force distribution. *Wind Energy* **2017**, *20*, 1083–1096. [[CrossRef](#)]
66. Troldborg, N. Actuator Line Modeling of Wind Turbine Wakes. Ph.D. Thesis, Technical University of Denmark, Lyngby, Denmark, 2009.
67. Martínez-Tossas, L.A.; Churchfield, M.J.; Yilmaz, A.E.; Sarlak, H.; Johnson, P.L.; Sørensen, J.N.; Meyers, J.; Meneveau, C. Comparison of four large-eddy simulation research codes and effects of model coefficient and inflow turbulence in actuator-line-based wind turbine modeling. *J. Renew. Sustain. Energy* **2018**, *10*, 033301. [[CrossRef](#)]
68. Jha, P.; Churchfield, M.; Moriarty, P.; Schmitz, S. Guidelines for Volume Force Distributions Within Actuator Line Modeling of Wind Turbines on Large-Eddy Simulation-Type Grids. *J. Sol. Energy Eng.* **2014**, *136*, 031003. [[CrossRef](#)]
69. Martínez-Tossas, L.A.; Meneveau, C. Filtered lifting line theory and application to the actuator line model. *J. Fluid Mech.* **2019**, *863*, 269–292. [[CrossRef](#)]
70. Meyer Forsting, A.R.; Pirrung, G.R.; Ramos-García, N. A vortex-based tip/smearing correction for the actuator line. *Wind Energy Sci.* **2019**, *4*, 369–383. [[CrossRef](#)]
71. Peskin, C.S. The immersed boundary method. *Acta Numer.* **2002**, *11*, 479–517. [[CrossRef](#)]
72. Yang, X.; Zhang, X.; Li, Z.; He, G.W. A smoothing technique for discrete delta functions with application to immersed boundary method in moving boundary simulations. *J. Comput. Phys.* **2009**, *228*, 7821–7836. [[CrossRef](#)]
73. Yang, X.; Kang, S.; Sotiropoulos, F. Computational study and modeling of turbine spacing effects in infinite aligned wind farms. *Phys. Fluids* **2012**, *24*, 115107. [[CrossRef](#)]
74. Schepers, J.; Schreck, S. Aerodynamic measurements on wind turbines. *Wiley Interdiscip. Rev. Energy Environ.* **2019**, *8*, e320. [[CrossRef](#)]
75. Politis, E.S.; Prospathopoulos, J.; Cabezon, D.; Hansen, K.S.; Chaviaropoulos, P.; Barthelmie, R.J. Modeling wake effects in large wind farms in complex terrain: The problem, the methods and the issues. *Wind Energy* **2012**, *15*, 161–182. [[CrossRef](#)]
76. Shapiro, C.R.; Gayme, D.F.; Meneveau, C. Filtered actuator disks: Theory and application to wind turbine models in large eddy simulation. *Wind Energy* **2019**, *22*, 1414–1420. [[CrossRef](#)]
77. Troldborg, N.; Zahle, F.; Réthoré, P.E.; Sørensen, N.N. Comparison of wind turbine wake properties in non-sheared inflow predicted by different computational fluid dynamics rotor models. *Wind Energy* **2015**, *18*, 1239–1250. [[CrossRef](#)]
78. Shen, W.Z.; Hansen, M.O.; Sørensen, J.N. Determination of the angle of attack on rotor blades. *Wind Energy* **2009**, *12*, 91–98. [[CrossRef](#)]
79. Shen, W.Z.; Hansen, M.O.; Sørensen, J.N. Determination of angle of attack (AOA) for rotating blades. In *Wind Energy*; Springer: New York, NY, USA, 2007; pp. 205–209.
80. Ramdin, S. Prandtl Tip Loss Factor Assessed. Master's Thesis, Delft University of Technology, Delft, The Netherlands, 2017.
81. Zhong, W.; Wang, T.G.; Zhu, W.J.; Shen, W.Z. Evaluation of tip loss corrections to AD/NS simulations of wind turbine aerodynamic performance. *Appl. Sci.* **2019**, *9*, 4919. [[CrossRef](#)]
82. Snel, H.; Schepers, J.; Montgomerie, B. The MEXICO project (Model Experiments in Controlled Conditions): The database and first results of data processing and interpretation. *J. Phys. Conf. Ser.* **2007**, *75*, 012014. [[CrossRef](#)]
83. Schepers, J.; Boorsma, K.; Cho, T.; Gomez-Iradi, S.; Schaffarczyk, P.; Jeromin, A.; Lutz, T.; Meister, K.; Stoevesandt, B.; Schreck, S.; et al. Mexnet (Phase 1): Analysis of Mexico Wind Tunnel measurements. In *Proceedings of the Final Report of IEA Task 29*; IEA: Paris, France, 2012.
84. Shen, W.Z.; Zhu, W.J.; Sørensen, J.N. Actuator line/Navier–Stokes computations for the MEXICO rotor: Comparison with detailed measurements. *Wind Energy* **2012**, *15*, 811–825. [[CrossRef](#)]
85. Shen, W.Z.; Zhu, W.J.; Yang, H. Validation of the Actuator Line Model for Simulating Flows Past Yawed Wind Turbine Rotors. *J. Power Energy Eng.* **2015**, *03*, 7–13. [[CrossRef](#)]
86. Stanly, R.; Martínez-Tossas, L.A.; Frankel, S.H.; Delorme, Y. Large-Eddy Simulation of a wind turbine using a Filtered Actuator Line Model. *J. Wind Eng. Ind. Aerodyn.* **2022**, *222*, 104868. [[CrossRef](#)]
87. Boorsma, K.; Schepers, J. New MEXICO experiment. In *Preliminary Overview with Initial Validation*; Technical Report ECN-E-14-048; ECN: Petten, The Netherlands, 2014.
88. Boorsma, K.; Schepers, J. Rotor experiments in controlled conditions continued: New Mexico. *J. Phys. Conf. Ser.* **2016**, *753*, 022004. [[CrossRef](#)]
89. Krogstad, P.Å.; Sætran, L. Wind turbine wake interactions; results from blind tests. *J. Phys. Conf. Ser.* **2015**, *625*, 012043. [[CrossRef](#)]
90. Krogstad, P.Å.; Eriksen, P.E. “Blind test” calculations of the performance and wake development for a model wind turbine. *Renew. Energy* **2013**, *50*, 325–333. [[CrossRef](#)]
91. Pierella, F.; Krogstad, P.Å.; Sætran, L. Blind Test 2 calculations for two in-line model wind turbines where the downstream turbine operates at various rotational speeds. *Renew. Energy* **2014**, *70*, 62–77. [[CrossRef](#)]
92. Krogstad, P.Å.; Sætran, L.; Adaramola, M.S. “Blind Test 3” calculations of the performance and wake development behind two in-line and offset model wind turbines. *J. Fluids Struct.* **2015**, *52*, 65–80. [[CrossRef](#)]
93. Bartl, J.; Sætran, L. Blind test comparison of the performance and wake flow between two in-line wind turbines exposed to different turbulent inflow conditions. *Wind Energy Sci.* **2017**, *2*, 55–76. [[CrossRef](#)]

94. Mühle, F.; Schottler, J.; Bartl, J.; Futrzynski, R.; Evans, S.; Bernini, L.; Schito, P.; Draper, M.; Guggeri, A.; Kleusberg, E.; et al. Blind test comparison on the wake behind a yawed wind turbine. *Wind Energy Sci.* **2018**, *3*, 883–903. [[CrossRef](#)]
95. Chamorro, L.P.; Porté-Agel, F. Effects of thermal stability and incoming boundary-layer flow characteristics on wind-turbine wakes: A wind-tunnel study. *Bound.-Layer Meteorol.* **2010**, *136*, 515–533. [[CrossRef](#)]
96. Chamorro, L.P.; Porté-Agel, F. Turbulent flow inside and above a wind farm: A wind-tunnel study. *Energies* **2011**, *4*, 1916–1936. [[CrossRef](#)]
97. Chamorro, L.; Hill, C.; Morton, S.; Ellis, C.; Arndt, R.; Sotiropoulos, F. On the interaction between a turbulent open channel flow and an axial-flow turbine. *J. Fluid Mech.* **2013**, *716*, 658–670. [[CrossRef](#)]
98. Nathan, J.; Masson, C.; Dufresne, L. Near-wake analysis of actuator line method immersed in turbulent flow using large-eddy simulations. *Wind Energy Sci.* **2018**, *3*, 905–917. [[CrossRef](#)]
99. Réthoré, P.E.; van der Laan, P.; Troldborg, N.; Zahle, F.; Sørensen, N.N. Verification and validation of an actuator disc model. *Wind Energy* **2014**, *17*, 919–937. [[CrossRef](#)]
100. Stevens, R.J.; Martínez-Tossas, L.A.; Meneveau, C. Comparison of wind farm large eddy simulations using actuator disk and actuator line models with wind tunnel experiments. *Renew. Energy* **2018**, *116*, 470–478. [[CrossRef](#)]
101. Lignarolo, L.E.; Mehta, D.; Stevens, R.J.; Yilmaz, A.E.; van Kuik, G.; Andersen, S.J.; Meneveau, C.; Ferreira, C.J.; Ragni, D.; Meyers, J.; et al. Validation of four LES and a vortex model against stereo-PIV measurements in the near wake of an actuator disc and a wind turbine. *Renew. Energy* **2016**, *94*, 510–523. [[CrossRef](#)]
102. Rethore, P.E.M.; Sørensen, N.N.; Zahle, F.; Johansen, J. Comparison of an actuator disc model with a full rotor CFD model under uniform and shear inflow condition. In Proceedings of the 4th PhD Seminar on Wind Energy in Europe, Magdeburg, Germany, 1 October 2008.
103. Howland, M.F.; Bossuyt, J.; Martínez-Tossas, L.A.; Meyers, J.; Meneveau, C. Wake structure in actuator disk models of wind turbines in yaw under uniform inflow conditions. *J. Renew. Sustain. Energy* **2016**, *8*, 043301. [[CrossRef](#)]
104. Sarmast, S.; Shen, W.Z.; Zhu, W.J.; Mikkelsen, R.F.; Breton, S.P.; Ivanell, S. Validation of the actuator line and disc techniques using the New MEXICO measurements. *J. Phys. Conf. Ser.* **2016**, *753*, 032026. [[CrossRef](#)]
105. Lignarolo, L.; Ragni, D.; Ferreira, C.; Van Bussel, G. Experimental comparison of a wind-turbine and of an actuator-disc near wake. *J. Renew. Sustain. Energy* **2016**, *8*, 023301. [[CrossRef](#)]
106. Nilsson, K.; Shen, W.Z.; Sørensen, J.N.; Breton, S.P.; Ivanell, S. Validation of the actuator line method using near wake measurements of the MEXICO rotor. *Wind Energy* **2015**, *18*, 499–514. [[CrossRef](#)]
107. Nathan, J. Application of Actuator Surface Concept in LES Simulations of the Near Wake of Wind Turbines. Ph.D Thesis, École de Technologie Supérieure, Montréal, QC, Canada, 2018.
108. Breton, S.P.; Watters, C.S.; Masson, C.; Gomez-Iradi, S.; Munduate, X. On the prediction of tip vortices in the near wake of the MEXICO rotor using the actuator surface method. *Int. J. Eng. Syst. Model. Simul.* **2012**, *4*, 11–26. [[CrossRef](#)]
109. Sørensen, J.N. Instability of helical tip vortices in rotor wakes. *J. Fluid Mech.* **2011**, *682*, 1–4. [[CrossRef](#)]
110. Ivanell, S.; Mikkelsen, R.; Sørensen, J.N.; Henningson, D. Stability analysis of the tip vortices of a wind turbine. *Wind Energy* **2010**, *13*, 705–715. [[CrossRef](#)]
111. Yang, X.; Hong, J.; Barone, M.; Sotiropoulos, F. Coherent dynamics in the rotor tip shear layer of utility-scale wind turbines. *J. Fluid Mech.* **2016**, *804*, 90–115. [[CrossRef](#)]
112. Hong, J.; Toloui, M.; Chamorro, L.P.; Guala, M.; Howard, K.; Riley, S.; Tucker, J.; Sotiropoulos, F. Natural snowfall reveals large-scale flow structures in the wake of a 2.5-MW wind turbine. *Nat. Commun.* **2014**, *5*, 1–9. [[CrossRef](#)] [[PubMed](#)]
113. Barthelmeie, R.J.; Rathmann, O.; Frandsen, S.T.; Hansen, K.; Politis, E.; Prospathopoulos, J.; Rados, K.; Cabezón, D.; Schlez, W.; Phillips, J.; et al. Modelling and measurements of wakes in large wind farms. *J. Phys. Conf. Ser.* **2007**, *75*, 012049. [[CrossRef](#)]
114. Wang, J.; Wang, C.; Campagnolo, F.; Bottasso, C.L. Wake behavior and control: Comparison of LES simulations and wind tunnel measurements. *Wind Energy Sci.* **2019**, *4*, 71–88. [[CrossRef](#)]
115. Aubrun, S.; Loyer, S.; Hancock, P.E.; Hayden, P. Wind turbine wake properties: Comparison between a non-rotating simplified wind turbine model and a rotating model. *J. Wind Eng. Ind. Aerodyn.* **2013**, *120*, 1–8. [[CrossRef](#)]
116. Aubrun, S.; Espana, G.; Loyer, S.; Hayden, P.; Hancock, P. Is the actuator disc concept sufficient to model the far-wake of a wind turbine? In *Progress in Turbulence and Wind Energy IV*; Springer: New York, NY, USA, 2012; pp. 227–230.
117. Porté-Agel, F.; Wu, Y.T.; Lu, H.; Conzemi, R.J. Large-eddy simulation of atmospheric boundary layer flow through wind turbines and wind farms. *J. Wind Eng. Ind. Aerodyn.* **2011**, *99*, 154–168. [[CrossRef](#)]
118. Larsen, T.J.; Madsen, H.A.; Larsen, G.C.; Hansen, K.S. Validation of the dynamic wake meander model for loads and power production in the Egmond aan Zee wind farm. *Wind Energy* **2013**, *16*, 605–624. [[CrossRef](#)]
119. Yang, X.; Sotiropoulos, F. A review on the meandering of wind turbine wakes. *Energies* **2019**, *12*, 4725. [[CrossRef](#)]
120. Mao, X.; Sørensen, J. Far-wake meandering induced by atmospheric eddies in flow past a wind turbine. *J. Fluid Mech.* **2018**, *846*, 190–209. [[CrossRef](#)]
121. Gupta, V.; Wan, M. Low-order modelling of wake meandering behind turbines. *J. Fluid Mech.* **2019**, *877*, 534–560. [[CrossRef](#)]
122. Yang, X.; Sotiropoulos, F. Wake characteristics of a utility-scale wind turbine under coherent inflow structures and different operating conditions. *Phys. Rev. Fluids* **2019**, *4*, 024604. [[CrossRef](#)]
123. Porté-Agel, F.; Wu, Y.T.; Chen, C.H. A numerical study of the effects of wind direction on turbine wakes and power losses in a large wind farm. *Energies* **2013**, *6*, 5297–5313. [[CrossRef](#)]



124. Wu, Y.T.; Porté-Agel, F. Modeling turbine wakes and power losses within a wind farm using LES: An application to the Horns Rev offshore wind farm. *Renew. Energy* **2015**, *75*, 945–955. [[CrossRef](#)]
125. Joulin, P.A.; Mayol, M.L.; Masson, V.; Blondel, F.; Rodier, Q.; Cathelain, M.; Lac, C. The actuator line method in the meteorological LES model meso-NH to analyze the horns rev 1 wind farm photo case. *Front. Earth Sci.* **2020**, *7*, 350. [[CrossRef](#)]
126. Yang, X.; Milliren, C.; Kistner, M.; Hogg, C.; Marr, J.; Shen, L.; Sotiropoulos, F. High-fidelity simulations and field measurements for characterizing wind fields in a utility-scale wind farm. *Appl. Energy* **2021**, *281*, 116115. [[CrossRef](#)]
127. Yang, D.; Meneveau, C.; Shen, L. Large-eddy simulation of offshore wind farm. *Phys. Fluids* **2014**, *26*, 025101. [[CrossRef](#)]
128. Churchfield, M.J.; Lee, S.; Moriarty, P.J.; Hao, Y.; Lackner, M.A.; Barthelmie, R.; Lundquist, J.K.; Oxley, G. A comparison of the dynamic wake meandering model, large-eddy simulation, and field data at the egmond aan Zee offshore wind plant. In Proceedings of the 33rd Wind Energy Symposium, Kissimmee, FL, USA, 5–9 January 2015; p. 0724.
129. Yang, D.; Meneveau, C.; Shen, L. Effect of downwind swells on offshore wind energy harvesting—a large-eddy simulation study. *Renew. Energy* **2014**, *70*, 11–23. [[CrossRef](#)]
130. The OpenFOAM Foundation. OpenFOAM. 25 August 2022. Available online: <https://openfoam.org/> (accessed on 4 September 2022).
131. Hasager, C.B.; Rasmussen, L.; Peña, A.; Jensen, L.E.; Réthoré, P.E. Wind farm wake: The Horns Rev photo case. *Energies* **2013**, *6*, 696–716. [[CrossRef](#)]
132. Yang, X.; Pakula, M.; Sotiropoulos, F. Large-eddy simulation of a utility-scale wind farm in complex terrain. *Appl. Energy* **2018**, *229*, 767–777. [[CrossRef](#)]
133. Liu, L.; Stevens, R.J. Effects of two-dimensional steep hills on the performance of wind turbines and wind farms. *Bound.-Layer Meteorol.* **2020**, *176*, 251–269. [[CrossRef](#)]
134. Eriksson, O.; Lindvall, J.; Breton, S.P.; Ivanell, S. Wake downstream of the Lillgrund wind farm—A Comparison between LES using the actuator disc method and a Wind farm Parametrization in WRF. *J. Phys. Conf. Ser.* **2015**, *625*, 012028. [[CrossRef](#)]
135. Wang, Q.; Luo, K.; Yuan, R.; Zhang, S.; Fan, J. Wake and performance interference between adjacent wind farms: Case study of Xinjiang in China by means of mesoscale simulations. *Energy* **2019**, *166*, 1168–1180. [[CrossRef](#)]
136. Wang, Q.; Luo, K.; Wu, C.; Mu, Y.; Tan, J.; Fan, J. Diurnal impact of atmospheric stability on inter-farm wake and power generation efficiency at neighboring onshore wind farms in complex terrain. *Energy Convers. Manag.* **2022**, *267*, 115897. [[CrossRef](#)]
137. Pettas, V.; Kretschmer, M.; Clifton, A.; Cheng, P.W. On the effects of inter-farm interactions at the offshore wind farm Alpha Ventus. *Wind Energy Sci.* **2021**, *6*, 1455–1472. [[CrossRef](#)]
138. Dong, G.; Li, Z.; Qin, J.; Yang, X. How far the wake of a wind farm can persist for? *Theor. Appl. Mech. Lett.* **2022**, *12*, 100314. [[CrossRef](#)]
139. Zehtabiyani-Rezaie, N.; Iosifidis, A.; Abkar, M. Data-driven fluid mechanics of wind farms: A review. *J. Renew. Sustain. Energy* **2022**, *14*, 032703. [[CrossRef](#)]
140. Yang, X. Towards the development of a wake meandering model based on neural networks. *J. Phys. Conf. Ser.* **2020**, *1618*, 062026. [[CrossRef](#)]
141. Wang, L.; Xie, J.; Luo, W.; Wang, Z.; Zhang, B.; Chen, M.; Tan, A.C. Effectiveness of data-driven wind turbine wake models developed by machine/deep learning with spatial-segmentation technique. *Sustain. Energy Technol. Assess.* **2022**, *53*, 102499. [[CrossRef](#)]
142. Iungo, G.V.; Santoni-Ortiz, C.; Abkar, M.; Porté-Agel, F.; Rotea, M.A.; Leonardi, S. Data-driven reduced order model for prediction of wind turbine wakes. *J. Phys. Conf. Ser.* **2015**, *625*, 012009. [[CrossRef](#)]